



Title	An integrated geophysical study of Vestbakken Volcanic Province, western Barents Sea continental margin, and adjacent oceanic crust
Author(s)	Libak, Audun; Mjelde, Rolf; Keers, Henk; Faleide, Jan Inge; Murai, Yoshio
Citation	Marine Geophysical Research, 33(2), 185-207 https://doi.org/10.1007/s11001-012-9155-3
Issue Date	2012-06
Doc URL	http://hdl.handle.net/2115/49692
Rights	The final publication is available at www.springerlink.com
Type	article (author version)
File Information	MGR33-2_185-207.pdf



[Instructions for use](#)

**An Integrated Geophysical Study of Vestbakken Volcanic Province,
Western Barents Sea Continental Margin, and Adjacent Oceanic Crust**

Audun Libak^{1*}, Rolf Mjelde¹, Henk Keers¹, Jan Inge Faleide² and Yoshio Murai³

¹ Department of Earth Science, University of Bergen, Allegaten 41, 5007 Bergen, Norway

² Department of Geosciences, University of Oslo, PObox 1047 Blindern, 0316 Oslo, Norway

³ Institute of Seismology and Volcanology, Hokkaido University, Sapporo, Japan.

* Corresponding author:
Audun Libak
Department of Earth Science
University of Bergen
Allegaten 41, 5007 Bergen
Norway
audun.libak@geo.uib.no
Tel.: +47 55588131

Abstract

This paper describes results from a geophysical study in the Vestbakken Volcanic Province, located on the central parts of the western Barents Sea continental margin, and adjacent oceanic crust in the Norwegian-Greenland Sea. The results are derived mainly from interpretation and modeling of multichannel seismic, ocean bottom seismometer and land station data along a regional seismic profile. The resulting model shows oceanic crust in the western parts of the profile. This crust is buried by a thick Cenozoic sedimentary package. Low velocities in the bottom of this package indicate overpressure. The igneous oceanic crust shows an average thickness of 7.2 km with the thinnest crust (5-6 km) in the southwest and the thickest crust (8-9 km) close to the continent-ocean boundary (COB). The thick oceanic crust is probably related to high mantle temperatures formed by brittle weakening and shear heating prior to continental breakup. The COB is interpreted in the central parts of the profile where the velocity structure and Bouguer anomalies change significantly. East of the COB Moho depths increase while the vertical velocity gradient decreases. Below the assumed center for Early Eocene volcanic activity the model shows increased velocities in the crust. These increased crustal velocities are interpreted to represent Early Eocene mafic feeder dykes. East of the zone of volcanoes velocities in the crust decrease and sedimentary velocities are observed at depths of more than 10 km. The amount of crustal intrusions is much lower in this area than farther west. East of the Knølegga Fault crystalline basement velocities are brought close to the seabed. This fault marks the eastern limit of thick Cenozoic and Mesozoic packages on central parts of the western Barents Sea continental margin.

Keywords: Seismic modeling, Ocean bottom seismometer, Mafic feeder dykes, Oceanic and continental crust, Vestbakken Volcanic Province

1. Introduction

Continental margins are the key to understand the processes responsible for continental breakup and the formation of deep ocean basins. The sedimentary and magmatic rocks on continental margins provide valuable information about the tectonomagmatic evolution of these areas. More than 40 years of research have resulted in a good understanding of the formation of continental margins. Even though most continental margins are rifted, several authors have discussed sheared (or transform) continental margins (e.g. Scrutton 1979; Lorenzo 1997). Such margins form where breakup along a rift zone terminates in a continental strike-slip zone. The relative plate motions are then taken up as shear motions in the strike-slip system and an abrupt transition from relatively thick continental crust to thin oceanic crust is produced.

The central part of the western Barents Sea continental margin (Fig. 1) is classified as a rifted continental margin segment located between two predominantly sheared segments (Eldholm et al. 1987). It is dominated by the Early Eocene Vestbakken Volcanic Province (VVP) (Fig. 1) where extensive volcanism occurred in Early Eocene resulting in volcanic flows of large areal extent (Faleide et al. 1988). VVP is the only area on the western Barents Sea continental margin where significant volumes of Cenozoic extrusives are observed. The basaltic flows are acoustically opaque and can thus cause problems in the seismic imaging of underlying rocks. Therefore, the crustal structure below the basalt is not well known.

In 2008 a regional ocean bottom seismometer (OBS) profile, called BIS-2008, was acquired in VVP and adjacent oceanic crust (Fig. 2). 12 short period OBSs, one broadband OBS and several temporary land stations on Bear Island recorded airgun shots and TNT charges fired along the profile. This profile was acquired in an area which has been previously

studied only by multichannel seismic (MCS) data and potential field data. Hence, BIS-2008 is the first deep wide-angle seismic profile in VVP.

Czuba et al. (2011) modeled the data recorded along BIS-2008, but did not include older MCS data in their work. They found a shallow granitic basement and a thin sedimentary package in western parts of the province. Along the continental margin to the south of VVP, a sedimentary package more than 12 km thick is observed (Breivik et al. 1998; Mjelde et al. 2002). If the interpretations in Czuba et al. (2011) are correct VVP is underlain by a granitic basement high, a fact that would be surprising based on plate tectonic models and the presence of the deep surrounding sedimentary basins. The same authors reported the presence of a high velocity body that constitutes the whole crystalline crust below the Cenozoic sedimentary package in the continent-ocean transition zone on the western side of the province. This body was interpreted as serpentinized peridotites generated during continental breakup. Serpentinized peridotites are formed when magmatic activity is limited (e.g. Minshull et al. 1998) and are not expected in such a narrow area located between a magmatic province and 8-9 km thick oceanic crust.

The objective of this paper is to investigate the crustal structure along the BIS-2008 profile in more detail using available MCS data in addition to the wide-angle data used by Czuba et al. (2011). We wanted to verify if the same results are obtained when we include more data constraints and apply different modeling methods.

2. Geology

2.1 Regional geological evolution

Prior to Late Cretaceous the areas which today constitute the central parts of the western Barents Sea continental margin and Bear Island were located off northeast Greenland, close to

the Wandel Sea (Smith 2000) (Fig. 1). The translation of Bear Island and surrounding regions away from northeast Greenland started in Late Cretaceous along a large dextral continental strike-slip zone (Faleide et al. 1993). This continental strike-slip zone, often called the De Geer Zone, was located between the western Barents Sea/Svalbard and northeast Greenland, and extended from northern Norway to the Arctic Ocean. Sedimentary basins with thick packages of Cretaceous and Cenozoic rocks developed within the De Geer Zone (Faleide et al. 1993). The Harstad Basin and the Sørvestsnaget Basin (Fig. 2) on the western Barents Sea margin and the Wandel Sea Basin (Håkansson and Pedersen 2001) on the NE Greenland margin (Fig. 1) are examples of such basins.

The western Barents Sea margin evolved along the De Geer Zone during the Cenozoic. Continental breakup occurred south of Greenland-Senja Fracture Zone at the Paleocene-Eocene transition (~55 Ma) (Faleide et al. 2008). Since the relative plate motions were parallel to the strike-slip system the breakup did not propagate into the southwestern Barents Sea, but instead the movements were taken up as shear motions in the De Geer Zone. Irregularities in the strike-slip zone resulted in generation of different margin segments on the western Barents Sea margin. In areas where the relative motion was close to pure strike-slip, sheared segments were formed. The Senja Margin and Hornsund Margin (Fig. 1) are considered as predominantly sheared segments (Faleide et al. 2008). Southwest of Bear Island, however, a jump in the strike-slip system resulted in a pull-apart setting. This pull-apart regime generated a predominantly rifted segment dominated by the Early Eocene Vestbakken Volcanic Province (Fig. 1). It is interesting to note that the western Barents Sea continental margin developed to the west of the Caledonian suture zone which is most likely located east of Bear Island (Barrère et al. 2009; Barrère et al. 2011).

In Earliest Oligocene (Chron 13) the relative plate motion between Greenland and Eurasia changed, resulting in an extensional component along the initially sheared segments

(Faleide et al. 2008). This change resulted in opening of the Fram Strait (Fig. 1) and a deepwater connection to the Arctic Ocean basin in Early Miocene (Engen et al. 2008; Jakobsson et al. 2007). The extensional component also detached two continental slivers from the western Barents margin: the East Greenland Ridge (Døssing et al. 2008) and the Hovgård Ridge (Myhre et al. 1982) (Fig. 1).

Uplift and erosion of the Barents Sea in Late Cenozoic times, accompanied by the northern hemisphere glaciations in Late Pliocene and Pleistocene, resulted in the deposition of a thick sedimentary wedge on the continental margin and adjacent oceanic crust (Faleide et al. 1996; Fiedler and Faleide 1996; Hjelstuen et al. 1996). Cenozoic erosion was in the order of 2-3 km on Svalbard and the Svalbard Platform (Fig. 1) and 1-2 km south of Bear Island (Dimakis et al. 1998). The depocenters for these sediments were the Bear Island Fan west of the Senja Margin (Fiedler and Faleide 1996) and the Storfjorden Fan west of the Hornsund Margin (Hjelstuen et al. 1996) (Fig. 1).

2.2 Vestbakken Volcanic Province

VVP (Fig. 3) is located on the central parts of the western Barents Sea continental margin and is part of the central rifted segment (Faleide et al. 1993). The province is defined by a high reflectivity, acoustically opaque horizon in the multichannel seismic images at ~2-5 s two-way travel time (TWT). This high reflectivity horizon has been drilled and the well data imply that it represents volcanic flows of Early Eocene age, generated close to the time of continental breakup south of Greenland-Senja Fracture Zone (Knutsen and Larsen 1997).

Gabrielsen et al. (1990) defined VVP as the area between 73°30' and 74°30' N and between the continent-ocean boundary and approximately 17°E. MCS data do, however, show Early Eocene basaltic flows as far south as 73°N (Fig. 3). In the northwestern parts of the province several buried mounds are observed. These mounds are interpreted as buried

volcanoes of Early Eocene age (volcano V1) and Early Oligocene age (volcanoes V2 and V3) (Faleide et al. 1988) (Fig. 3).

The Cenozoic evolution of VVP is documented in several papers (Eidvin et al. 1998; Faleide et al. 1988; Richardsen et al. 1991; Ryseth et al. 2003; Sættem et al. 1994). The unpublished work by Jebsen (1998) is probably the most extensive study of the province. All of these studies reported several tectonic and volcanic events during the Cenozoic. As many as eight tectonic and three volcanic events may have occurred (Faleide et al. 2008).

The early Eocene volcanic activity was probably centered in the western parts of the province (Jebsen 1998), in the areas close to the Eocene volcano (V1 Fig. 3). The volcanic extrusives flowed in all directions from this eruption center resulting in the generation of the opaque, high amplitude horizon that defines VVP today (Fig. 3). The Early Eocene volcanic flows may initially have covered a much larger area, but later tectonic activity and erosion have determined the present distribution (Faleide et al. 1988). The basaltic flows are also observed on the conjugate margin offshore NE Greenland (Hinz et al. 1993).

Thick sedimentary packages of Middle-Late Eocene age are present above the volcanic flows in most of the province proving that it was a major sedimentary basin at this time. The uplifted Stappen High was the most important source area (Richardsen et al. 1991; Ryseth et al. 2003).

Two large fault zones have been especially important in the Cenozoic development of VVP. The Knølegga Fault (Gabrielsen et al. 1990) (Fig. 3) is the easternmost of these fault zones. It is located east of the volcanic province and constitutes the western limit of the Stappen High. The other fault zone, called Central Fault Zone (CFZ), is located at $\sim 17^{\circ}\text{E}$ (Fig. 3). It marks a boundary between Eocene seabed sediments in the east and Pliocene-Pleistocene seabed sediments in the west (Sættem et al. 1994). This fault zone is often

considered as the eastern limit of VVP, but volcanic products are also observed east of this fault zone (Faleide et al. 1988).

A regional uplift of VVP and the rest of the western Barents Sea occurred sometime between Middle Miocene and Middle Pliocene. The uplift was probably strongest in the west as manifested by the fact that the base of the Pliocene-Pleistocene sedimentary wedge truncates progressively older sedimentary rocks towards the west in the province (Eidvin et al. 1998).

The pre-Cenozoic geology of the province is less well understood, mainly because of the problems with sub-basalt seismic imaging. In the end of the 1980s several authors proposed that VVP is underlain by thick oceanic crust and that the continent-ocean boundary was located close to the CFZ (Eldholm et al. 1987; Faleide et al. 1988). Drilling of exploration well 7316/5-1 (Fig. 2) in 1992, however, showed sedimentary rocks of Late Cretaceous (Maastrichtian) age below the volcanic flows (Knutsen and Larsen 1997; Ryseth et al. 2003), proving that at least the eastern parts of the province represent stretched continental crust covered by pre-breakup sedimentary rocks. Faleide et al. (1991) suggested that the outer parts of the province are thick oceanic crust and the inner parts are stretched continental crust covered by a mixture of volcanics and sediments. The same authors described the presence of two deep reflectors in the province. The upper reflector is located at ~17 km depth and was interpreted as the top of an underplated crustal unit. The lower reflector, located at ~23 km depth, was interpreted as Moho. An interpretation of such an underplated body implies that VVP can represent a volcanic rifted margin, although it lacks the characteristic seaward dipping reflectors.

More recent studies suggest that the whole province is underlain by stretched continental crust (Breivik et al. 1999; Engen et al. 2008). This was also the conclusion of Czuba et al. (2011) who modeled a continental crust increasing in thickness from west to east

in the province. They also observed a 3-4 km thick high velocity layer in the lower crust, interpreted to be a result of mafic intrusions, and an unexpectedly shallow crystalline basement in the western parts of the province. Clark et al. (2009) observed a Moho at ~21 km depth in central parts of the province and reported no signs of high velocities at middle and lower crustal levels, implying continental crust.

3. Data and methods

3.1. Database

This study is mainly based on interpretation and modeling of seismic data. Gravity and magnetic data are used qualitatively to support geological interpretations. Furthermore results from published studies are integrated in the work.

The MCS data used is a set of regional 2D profiles acquired on behalf of the Norwegian Petroleum Directorate (Fig. 2). The MCS data coverage is dense in the VVP. On the oceanic crust and east of the CFZ the data coverage is sparse. The MCS data show the seismic stratigraphy and structural elements down to the Early Eocene volcanic flows in the volcanic province and down to the top oceanic basement on the oceanic crust (Fig. 4). We will use the term “top basalt” to include both top oceanic basement and top volcanic flows in VVP throughout the rest of the paper.

Since the MCS data gives little or no information about the rocks below the top basalt horizon we used data recorded by ocean bottom seismometers (OBS) along the BIS-2008 profile (Fig. 2) in order to gain information about deeper structures. Along the entire length of this profile airgun shots were fired with 200 m shot spacing while TNT charges were fired with ~2 km spacing in the northeastern parts of the profile, between OBS 7 and Bear Island (Fig. 2). The seismic signals were recorded on 12 short period OBSs, one broadband OBS and

a number of temporary land stations at Bear Island (Fig. 2). The data acquisition is described in detail by Czuba et al. (2011). Figs. 5-7 show examples of airgun signals recorded on three different short period OBSs in different parts of the profile. Two other OBS profiles, P-07 (Clark et al. 2009) and BIN-2008 (Libak et al. 2012), were included as constraints for the deeper crustal structure (Fig. 2).

Gravity data and water depths were recorded continuously along BIS-2008 using a LaCoste-Romberg shipboard gravity meter and an echo sounder, respectively. The gravity data were corrected for drift using base ties in Tromsø, northern Norway, and in Longyearbyen, Svalbard. The observed linear drift was 0.36 mGal/day. The gravity data are presented as Bouguer anomalies where the water layer is replaced by densities of 2670 kg/m³. Also shown in this paper is a Bouguer anomaly map generated using data from Minakov (2011) (Fig. 8a).

The WDMAM grid (Maus et al. 2007) was used to generate a magnetic anomaly map (Fig. 8b) and the magnetic seafloor spreading anomalies interpreted by Engen et al. (2008) were used to determine age of the oceanic crust (Figs. 2, 8b).

The database described above makes it possible to get constraints on both shallow and deeper crustal structures. The MCS data constrain the shallow structure while the OBS data and potential field data give information about deeper (sub top basalt) structures.

3.2. Methods

In this work we have focused on seismic data. Because of the strong 3D structure of the study area it is not possible to do a proper 2D modeling of the potential field data. 3D modeling is beyond the scope of this paper, thus no potential field modeling was performed. In the following subsections we will explain the two different methods used to model seismic travel times.

3.2.1. Modeling seismic travel times using Rayinvr

The primary goal of this paper is to map the crustal and upper mantle structure along BIS-2008 (Fig. 2). In order to do so we created a P-wave velocity model from the travel times recorded on OBSs and land stations using the Rayinvr package (Zelt and Smith 1992).

Velocity models generated solely based on travel times recorded on widely spaced OBSs are non-unique. The velocity models become more unique when other types of data are included. We therefore included information from the MCS lines. The MCS lines (Fig. 2) allow us to find the TWT to the top basalt in crossing points with BIS-2008. Since the top basalt represents a first order velocity discontinuity it is important to know the geometry of this boundary during modeling of OBS data. TWT from the MCS data was converted to zero-offset OBS time by subtracting the one-way travel time in the water column.

Seabed depths were taken from the echo sounder data and the water layer was given a velocity of 1.48 km/s, a typical velocity for arctic seas. The geometry and velocity of the water layer was fixed during the modeling.

The modeling was done using a top-down strategy; we started with the sedimentary arrivals and the top basalt reflections (both from the MCS picks and from the OBS data) and when an acceptable fit was obtained for these arrivals we kept the structure above the top basalt reflector fixed during the rest of the modeling.

The velocity structure below the top basalt interface was generally obtained by forward modeling/inversion of refractions only, since clear deep reflections are rarely observed along the profile. Some constraints on velocities below the top basalt interface in VVP were available from well 7316/5-1 which penetrates the Early Eocene volcanic flows (Fig. 2). Here the sedimentary rocks below the top basalt have a velocity of ~4 km/s, but the occurrence of high velocity mafic intrusions at regular intervals increases the average velocity

closer to 5 km/s. We therefore kept velocities just below the top basalt in VVP between 4 and 5 km/s and this resulted in a good fit with the picked arrivals. Examples from the modeling of three different OBSs are shown in Figs. 5-7.

The purpose of the travel time modeling is to produce a geologically meaningful model that minimizes travel time residuals (difference between picked and calculated arrivals) and where rays can be traced for as many picks as possible (Zelt and Smith 1992). It is, however, meaningless to obtain travel time residuals less than the uncertainty of the picks. Therefore an appropriate measure of travel time fit is the normalized chi-square (Zelt and Forsyth 1994) which has a value of one if the travel time residual is equal to the pick uncertainty. A lower value implies overfitting, while values larger than one imply that the residuals are higher than the pick uncertainty. During the modeling we sought a normalized chi-square value of one.

3.2.2. Modeling first arrival travel times using Tomo2d

Velocity models obtained using Rayinvr have a tendency to be quite subjective since the modeler needs to assign picked phases to particular model layers (e.g. Minshull 2009). Moreover, it is difficult to get good estimates on model resolution and model parameter uncertainty using this method.

In first arrival seismic tomography (Korenaga et al. 2000; Zelt and Barton 1998) it is not necessary to specify the refracting layer for a given pick. The travel time residuals between picked and calculated first arrivals are used together with the partial derivatives of travel times with respect to model parameters to create the inverse problem, which is usually solved using the least squares method. Regularization in the form of smoothing or damping is used to stabilize the inversion.

We used the Tomo2d code (Korenaga et al. 2000) to run first arrival tomography on our picks. Before we could run the code we had to remove all secondary arrivals from our original picks. A total number of 5681 first arrival picks (86.5 % of the total number of picks) were used in the inversion. The PgP phase (Table 1) is the most important of the secondary arrivals together with some sedimentary arrivals. These secondary arrivals have a very good fit in the final Rayinvr model. The sedimentary velocity structure and top basalt boundary from the Rayinvr model were therefore used as input for the tomographic inversion. This upper part of the velocity structure did not change significantly during the inversion because of the good fit between calculated and observed travel times in the initial model.

A set of 1-D initial velocity models was constructed from the top basalt boundary down to a Moho with varying depth. The velocity just below the top basalt boundary was the same for all initial models so the crustal velocity gradient became a function of lower crustal velocity and Moho depth. A total number of 200 different starting models were generated. All of these models had a horizontal grid spacing of 1 km and a vertical grid spacing increasing from 0.1 km in the top to 1 km in the bottom of the model. A horizontal correlation length increasing from 5 km in the top to 20 km in the bottom of the model and a vertical correlation length increasing from 0.5 km in the top to 1 km in the bottom of the model were used as smoothing constraints. 15 iterations were applied for each starting model resulting in chi-squared values of ~ 1.0 for all final models. By taking the average of the resulting 200 models the final velocity model was created. The standard deviations of the model parameters in this model were also calculated using the 200 models obtained from the inversions.

The only variable in the inversions described above was the starting model. If we had chosen to vary also the travel times within the uncertainty interval (Zhang and Toksöz 1998) and the smoothing constraints, the final model and standard deviations would probably be

somewhat different. However, since the starting model is the most important variable, we claim that the applied method should give reliable estimates of velocity uncertainties.

4. Results

4.1 Velocity models

4.1.1. Rayinvr model

The final Rayinvr model (Fig. 9b) is divided into eight different layers. The subdivision of the model into different layers is primarily a result of the model parameterization where a linear interpolation is applied between velocity values in the top and bottom of the layers and between adjacent velocity nodes laterally. Some layers do therefore have very similar velocities and the only difference is a change in velocity gradient. In other places a single layer can show different velocities laterally. Such layers can represent different layers physically, but they were modeled as a single layer in order to avoid near vertical model boundaries at layer pinch outs which are not desirable during ray-tracing.

The sedimentary layers (Layers 2, 3 and 4) generally show low velocities. The exception is northeast of OBS 14 where velocities are higher. The velocity increases rapidly from ~1.7 km/s at the seabed to ~2.4 km/s 0.5 km below the seafloor. Below this depth the vertical velocity gradient is low and the velocity in the bottom of the sedimentary package is generally lower than 3 km/s. In the northeastern parts of the profile two lateral velocity changes are observed in the sedimentary units. The first is located at ~km 315 where velocities in Layer 3 increase to more than 3 km/s. This lateral velocity discontinuity correlates with the position of CFZ observed in the MCS data. At km 350 an abrupt lateral velocity increase is observed. Northeast of km 350 velocities are generally higher than 4 km/s.

The high velocities (>5.5 km/s) in Layer 3 east of this discontinuity may indicate that the layer represents crystalline crust in this area.

Layer 5 (the layer beneath the top basalt boundary) shows top velocities of 4.7-5.2 km/s between the start of the profile and km 220. Velocities in the bottom of the layer are 5.6-6.4 km/s in the same interval. Northeast of km 220 the top and bottom velocities are somewhat lower. At km 348 an abrupt change from 5.0 km/s to 6.0 km/s occurs. The vertical velocity gradient in the layer is generally significantly higher in the first 220 km of the profile than farther northeast. The top layer boundary shows two peaks at km 240 and km 270, corresponding to volcanoes V1 and V3, respectively (Figs. 3, 9b). The thickness of the layer is 2.0-4.4 km, the thicker part being below the volcanoes at km 240 and km 270.

Layer 6, with velocities in the range 5.6-6.8 km/s, is present in the model from km 200 to the northeastern end of the profile. The velocities are generally highest between km 200 and km 260 and lowest between km 300 and km 350. Northeast of km 350 the layer shows top velocities of 6.4 km/s and bottom velocities of 6.7 km/s. The thickness of the layer increases from the southwest to the northeast.

Velocities between 6.8 and 7.6 km/s characterize Layer 7. The layer is present between the start of the profile and km 340. The thickest part of the layer is at km 250 where the thickness reaches a value of ~ 12 km.

The deepest modeled layer, Layer 8, has velocities of 7.9 km/s and higher. The upper boundary of Layer 8 is located at ~ 10 km depth in the southwestern end and 27 km in the northeastern end. The increase in depth is not gradual and a staircase shape of the top layer boundary is observed. The strongest change occurs between km 190 and km 250. This change is also reflected in the Bouguer anomalies (Fig. 9a). Below the central parts of VVP the top of the layer is modeled at ~ 23 km depth (corresponding to a TWT of 8-9 s) before it drops to depths of 27 km northeast of km 340.

4.1.2 Tomo2d model

The final model from first arrival seismic tomography (Fig. 10a) shows many similarities with the Rayinvr model, though it is less rough due to the correlation lengths used to regularize the inversion. The southwestern parts of the profile show high vertical velocity gradients in the upper basement as manifested by the short distance between the 5 km/s and 7 km/s contours. Below the 7 km/s contour the vertical velocity gradient is lower. Mantle velocities (~8 km/s) are found at deeper levels (~15 km) than in the Rayinvr model. Northeast of km 200 the distance between the 6 km/s and 7 km/s contours increases, hence the velocity gradient is lower. Velocities lower than ~6.3 km/s remains at the same crustal depth also northeast of km 200. Below the Eocene volcano (V1 Fig. 10a) pull-ups in the velocity contours are observed. Northeast of km 275 depths to velocities larger than 6 km/s increases, in accordance with the Rayinvr model. Close to km 350 the depths to high velocities decrease significantly and low velocity rocks are absent east of this point.

4.2 Velocity model assessment

An assessment should be presented for models obtained from modeling of seismic travel time data in order to show how well the different parts of the model are constrained (Zelt 1999). The model assessment for the Rayinvr model is presented as a table with statistics for the traced rays and travel time fits (Table 2), a figure showing ray hits in the final velocity model (Fig. 9c) and a synthetic seismogram for a high quality OBS in the central parts of the profile (Fig. 11).

Rays were traced for 97.4 % of the total number of picks and normalized chi-squared values are close to one for most of the phases (Table 2). The exception is the PmP phase which we had problems to fit. The pick uncertainties used in the chi-squared calculations are

in most cases between 50 and 100 ms depending on how clear the arrivals appear on the seismograms. For some unclear, far offset arrivals a pick uncertainty of 150-200 ms was used.

Ray hits (Fig. 9c) tell us something about the reliability of the obtained results in different parts of the model. It does not, however, indicate the absolute uncertainties. It should therefore be regarded as a relative measure of the quality between different parts of the model. No information can be drawn from the seismic data in areas without ray coverage (grey areas in Fig. 9c). The ray coverage decreases from central parts of the profile towards the ends.

Because few reflections were observed in the OBS data the layer boundaries are generally not constrained by reflections, but are instead inserted in order to fit the first arrival refracted phases. Some reflections, however, are modeled and these reflective interfaces are shown as red line segments (Fig. 9b). One boundary that is generally well constrained by reflections, both from MCS and OBS data, is the velocity discontinuity that represents the top of layer 5 (top basalt). Reflections from this boundary are observed on most of the OBSs and on all MCS lines west of OBS 13. Since the velocity structure of the layers above this horizon is relatively well constrained by rays (Fig. 9c) the depth of this interface is considered well constrained with estimated uncertainties in the order of 0.2 km.

The velocity structure in the top of Layer 5 is well constrained by rays. The ray hits plot shows that rays are diving relatively deep in this layer, and the velocity gradient is therefore well resolved. The exception is southwest of OBS 2 and northeast of OBS 13.

The velocity of layer 6 is well constrained by rays from km 200 to km 320. Northeast of km 320 only the top layer velocities are constrained (Fig. 9c).

In layer 7 rays are turning only in the upper half of the layer. The velocity structure in the bottom of the layer is therefore uncertain. No rays dive in this layer east of km 290. The structure of the layer northeast of this point is based on a few Pn recordings from OBS 15 and the land stations and should therefore be considered very uncertain. The reason for the pinch

out of the layer and a deepening of the top of layer 8 in the end of the profile is based on the results from other studies which show depths to the base of the crust of more than 30 km below the Stappen High (Barrère et al. 2011), and the fact that the Bouguer anomalies are decreasing east of km 320 (Fig. 9a).

The lower layer, layer 8, is only constrained by rays in the top of the layer (Fig. 9c). A few PmP arrivals are modeled in VVP, but these arrivals were difficult to fit with a single reflecting interface. The best fit was obtained with a reflecting interface at ~23 km depth. The fitting problems can imply that the observed reflections originate from more discontinuous reflectors in the lower crust/upper mantle (such as mafic sills) and not from a continuous layer boundary.

A comparison between observed and synthetic seismogram for OBS 9 is shown in Fig. 11. The synthetic seismogram is calculated using the Rayinvr velocity model. The quality of the observed data was very good on this OBS and it is located in the central parts of the profile where the data coverage is high. The observed data are scaled by \sqrt{t} (t is time) to convert to theoretical 2-D amplitudes. The fit between the two seismograms is representative for most of the modeled OBSs.

Fig. 10b shows the standard deviation of model velocities with respect to the average model obtained using first-arrival seismic tomography (Fig. 10a). It is calculated by using the 200 different models obtained from the tomography. Gray areas have no ray coverage and are therefore unresolved by seismic data. The uncertainties are generally below 0.1 km/s down to 9 km depth. Below 9 km depth uncertainties are higher, but generally lower than 0.2 km/s. The exceptions are southwest of km 75 and northeast of km 325 where uncertainties exceed 0.2 km/s.

In order to test the resolution of our Tomo2d model we performed a checkerboard test (Fig. 12). The starting model shown in Fig. 12a was perturbed with an alternating pattern of

negative and positive velocity anomalies of 5 percent magnitude below the top basalt boundary (Fig. 12b). The anomalies were 30 km wide and 2.5 km thick. Synthetic data from the perturbed model was inverted using the model in Fig. 12a as the starting model. We used the same number of iterations and the same smoothing constraints as in the real data inversions described above. The result of the checkerboard test (Fig. 12c) shows that the pattern in the perturbed model is well reproduced between km 50 and km 300 at 6-15 km depth. The perturbations are somewhat smeared out and the perturbations are therefore of smaller amplitude in the inverted model. Based on the checkerboard test we conclude that the lateral velocity changes observed in the final velocity model between 6 and 15 km depth are well resolved. Below 15 km depth and in the ends of the profile the resolution is low.

The differences between the smooth Tomo2d model and the Rayinvr model (Fig. 13) should in theory not significantly exceed the standard deviations shown in Fig. 10b. Yet, differences exceed 0.3 km/s several places (Fig. 13). Most of these large difference values occur close to areas of abrupt velocity changes in the Rayinvr model. In the central parts of the layers, however, the differences are generally lower than 0.2 km/s matching the standard deviations in Fig. 10b. This pattern results from the smoothing constraints used in the tomography. Zones in the Rayinvr model with abrupt changes in velocity will appear as smooth velocity transitions in the Tomo2d model and this generates the local strong velocity differences in Fig. 13. If the differences resulting from the smoothing constraints are ignored, only one area of large differences remains. This is the area northeast of km 275 and below 15 km depth. Here the velocity differences are generally very large. As discussed earlier this is an area constrained only by a few unclear travel time picks. This area is therefore poorly constrained and we conclude that it is too uncertain to draw any geological conclusions.

5. Discussion

5.1 Structure of the oceanic crust west of Vestbakken Volcanic Province

The SW-most ~200 km of BIS-2008 has a velocity structure typical for oceanic crust. This is in accordance with published literature (Breivik et al. 1999; Czuba et al. 2011). The igneous oceanic crust is buried by a thick package of low-velocity Cenozoic sedimentary rocks (Layers 2, 3 and 4 in Fig. 9b). Since BIS-2008 to a large extent follows the interpretation of Chron 6 on the oceanic crust (Figs. 2 and 8b) we suggest that most of the sedimentary rocks between km 0 and km 200 must be younger than ~20 Ma (Cande and Kent 1995). Much of these sedimentary rocks were deposited in Late Pliocene and Pleistocene due to glacial erosion of the uplifted Barents Sea and deposition in the Bear Island Fan in the deep ocean basin (Fiedler and Faleide 1996).

The low velocities (<3 km/s) in the Cenozoic sedimentary package indicate high porosity. Low velocities were also observed by Jackson et al. (1990) and Mjelde et al. (2002) in the sedimentary rocks covering the oceanic crust west of the Senja Margin at 72°N. These results differ from observations on the Storfjorden Fan (Fig. 1) where significantly higher velocities (~4 km/s) are observed in the bottom of the sedimentary package (Hjelstuen et al. 1996; Libak et al. 2012). The low sedimentary velocities in the deeper parts of the Bear Island Fan suggest overpressure (e.g. Scott et al. 2009) in the sedimentary rocks. Overpressure in the Bear Island Fan is also indicated by the presence of mud volcanoes west of Senja Fracture Zone (Eldholm et al. 1999). This overpressure is probably not related to high sedimentation rates as the reported rates are lower in the Bear Island Fan than the Storfjorden Fan (Fiedler and Faleide 1996; Hjelstuen et al. 1996). We therefore suggest that the different pressures in the fans are related to lithology variations resulting from different sediment source areas.

According to this interpretation the Bear Island Fan consists of more fine grained, low permeability rocks than the Storfjorden Fan.

The total thickness of the igneous oceanic crust ranges from 5 to 9 km (Fig. 14a). It is thin (5-6 km) in the southwest (km 0 to km 75) and thick (> 8 km) between km 75 and km 200. Czuba et al. (2011) reported similar thickness values, though 1-2 km thinner in the southwestern parts of the profile.

The igneous crustal thickness between km 75 and km 200 is higher than the global average of 7.1 km (White et al. 1992). The thickest crust is found between km 75 and km 120 where the igneous thickness is estimated to 9 km. This is significantly thicker than most of the surrounding oceanic crust (Jackson et al. 1990; Kandilarov et al. 2010; Klingelhöfer et al. 2000; Libak et al. 2012). However, Mjelde et al. (2002) observed a 7-8 km thick oceanic crust west of the COB on the Senja margin and Kandilarov et al. (2010) reported areas with 7-8 km thick oceanic crust on the eastern side of the Knipovich Ridge interpreted as crust accreted at a magmatic dominated spreading segment. Modeling shows that a spreading ridge is able to produce an igneous crust thicker than 8 km only if mantle temperatures are higher than normal (Bown and White 1994). The Iceland mantle plume has been responsible for the creation of thick crust farther south in the Norwegian-Greenland Sea during continental breakup in Early Eocene (Mjelde et al. 2008; Parkin et al. 2007). The same plume was responsible for most of the magmatic activity in VVP. The plume activity, however, decreased resulting in the generation of oceanic crust with normal thickness at ~ 48 Ma, away from the plume center. Since the oldest oceanic crust along BIS-2008 is of Early Oligocene age (as indicated by the magnetic Chrons) it is unlikely that it was affected by the Iceland Plume, which experienced restricted activity at that time (Mjelde et al. 2009). Crust of similar age farther south on the Mohns Ridge, in areas closer to the Iceland Plume, is only 4 km thick (Klingelhöfer et al. 2000). We find it likely that the thick oceanic crust after breakup is related

to the proximity of the Senja Fracture Zone. Behn et al. (2007) showed that the mantle temperature in fracture zones can be high due to brittle weakening of the lithosphere. Such weakening reduces the viscosity and enhances passive upwelling of hot mantle material below the fracture zone. In addition shear heating can elevate temperatures in such zones. We suggest that the change in relative plate motion in Early Oligocene resulted in rifting of such a hot region along the Senja Fracture Zone. This might explain why high magma production occurred for the oldest oceanic crust along our profile. The increased thickness of the igneous crust between km 75 and km 120 may be attributed to the increased pulse from the Iceland Plume starting at c. 23 Ma (Mjelde et al. 2009).

The upper igneous layer (Layer 5 in Fig. 9b) is interpreted as oceanic layer 2. It shows top oceanic basement velocities ranging from 4.6 to 5.2 km/s, quite similar to the velocities (5.0-5.2 km/s) in the model by Czuba et al. (2011). These velocities are lower than the values (5.7-6.4 km/s) reported by Jackson et al. (1990) west of the Senja Margin and higher than the velocities (~3.2 km/s) described by Klingelhöfer et al. (2000) close to the Mohs Ridge at 72°N. The velocities are, however, similar to the oceanic layer 2B in the models by Klingelhöfer et al. (2000), suggesting that the thin oceanic layer 2A is altered along our profile. Alternatively layer 2A is present, but too thin to be observed in the OBS data. The thickness of the layer (2-4 km) (Fig. 14a) is higher than the global average of 2.11 ± 0.55 km reported by White et al. (1992). In the model by Czuba et al. (2011) oceanic layer 2 reaches thickness values of 3 km, but is generally thinner than in our model.

The lower igneous layer (Layer 7 in Fig. 9b), interpreted as oceanic layer 3, shows velocities in the range 6.8-7.7 km/s. The thickness and average velocities for this layer in the Rayinvr model is shown in Fig. 14. Klingelhöfer et al. (2000) reported average upper mantle velocities of ~7.7 km/s on the eastern side of the Mohs Ridge. The highest velocities in the bottom of oceanic layer 3 in our model may therefore represent mantle rocks. Hence, in some

cases, the oceanic crustal thickness may be slightly overestimated. The layer reaches a maximum thickness of 6-7 km between km 75 and km 125. A similar thickness in oceanic layer 3 is observed off axis on the ultraslow Knipovich Ridge (Kandilarov et al. 2010), on an expected magmatic center of this ridge. However, that crust has lower average velocities (~6.7 km/s) than in our model. Moreover, the thick crustal segment in Kandilarov et al. (2010) is relatively narrow (~30 km) while our thick crust is observed over an interval more than 100 km wide. Along axis seismic studies from the ultraslow Southwest Indian Ridge show that the magmatic segment centers are typically 20-30 km wide (Minshull et al. 2006). The thick oceanic layer 3 along BIS-2008 is therefore probably not caused by a normal magmatic dominated segment on an ultraslow ridge.

Upper mantle velocities are 7.9-8.1 km/s. This is in accordance with most surrounding oceanic mantle velocities (Breivik et al. 2003; Czuba et al. 2011; Kandilarov et al. 2010; Libak et al. 2012; Mjelde et al. 2002).

5.2 The continent-ocean boundary

A well-defined change in velocity structure is observed in both the Rayinvr model and the Tomo2d model around km 200 (Figs. 9b, 10a). This area also shows the largest gradients in the Bouguer anomalies (Figs. 7a, 8a). The change in velocity is mainly observed in the velocity gradients at crustal levels where velocities exceed 6 km/s. West of km 200 the distance between the 6 km/s and 7 km/s contours generally is less than 2 km (Fig. 10a). East of km 200 depths to the 7 km/s contour increase rapidly while the 6 km/s contour stays at the same levels, causing a reduction in vertical velocity gradients. In addition Moho depth increases east of km 200. Since the model is well resolved in this area (Figs. 10b, 12c) and similar results were obtained with two different modeling approaches, we conclude that the velocity changes described above must be real.

On the MCS lines (Fig. 15) an escarpment-like feature is interpreted as the continent-ocean boundary (Faleide et al. 1993). This escarpment marks the boundary between continuous, high amplitude basalt flows in the east and rough oceanic basement in the west. On MCS lines close to our profile we observe a termination of the volcanic flows from the Eocene volcano (V1, Fig. 3) in the same area as the major change in velocity structure at km 200.

We interpret the abrupt changes in velocities, reflection character and gravity anomalies at ~km 200 as the COB. The reduction in velocity gradients in the crust to the east of this boundary is probably caused by an increased amount of sedimentary rocks and felsic igneous rocks in the crust. This crust most likely consists of heavily intruded continental crust while the crust west of the COB is purely mafic (oceanic).

Our modeling results show that the high velocity body presented by Czuba et al. (2011) in the continent-ocean transition zone is not necessary to fit the data. It is possible to obtain a good fit with a rough top basalt boundary at the COB (Figs. 9b, 10a). However, we cannot exclude the results obtained by these authors since the fit is equally good for both models. This demonstrates that more work is necessary in order to resolve the nature of the crust in this zone. A denser OBS spacing (<5 km) and coincident MCS data would probably provide the resolution needed in order to resolve the crust in this area.

5.3 Crustal structure in Vestbakken Volcanic Province

Based on the interpretation of the COB we argue that the crust east of km 200 represents thinned and intruded continental crust. Continental crustal thickness increases from west to east whereas the average crustal velocity decreases (Figs. 9b, 10a). The strong thickening of the crust just east of the COB is primarily caused by increased volumes of rocks with velocities higher than 6.4 km/s. Such velocities are typical for both igneous rocks containing

mafic material and high grade metamorphic rocks (Christensen and Mooney 1995). To the east of Bear Island, in areas closer to the assumed Caledonian suture, no evidence for high velocity crust is observed (Breivik et al. 2005). Hence, we find it unlikely that the increased velocities near the COB are caused by high grade metamorphism during the Caledonian Orogeny. The strong correlation between the Eocene and Oligocene volcanoes and high crustal velocities, especially the strong pull-up in the velocity contours below the Eocene volcano (V1 Fig. 10a), favor an interpretation of mafic material as the cause for elevated velocities close to the COB.

A strong positive anomaly is observed in the magnetic data in the area where the Eocene volcanic center is located (Figs. 8b, 9a) and it correlates with the pull-ups in velocity contours below V1 along BIS-2008. This is the only strong positive magnetic anomaly on the western Barents Sea continental margin (Fig. 8b), proving that this zone has a unique crustal structure. A similar combination of positive magnetic anomalies and pull-ups in the velocity contours, accompanied by high seismic crustal reflectivity, is reported close to the coast in Namibia (Bauer et al. 2003). These zones were interpreted as local areas of strongly intruded crust. In our OBS data the strongest deep crustal reflections are observed on OBS 9 and 10 (e.g. Fig. 6a), in the area where the high velocities and positive magnetic anomaly are observed. The strong similarities with the features in Namibia and the strong correlation with the Cenozoic volcanoes point to a crust strongly intruded by mafic material in the area below the positive magnetic anomaly in the northwestern parts of VVP. The intrusion density is probably highest just below the Early Eocene volcanic center where mafic feeder dykes penetrate the whole crust (Fig. 10a). The relatively high velocities on each side of the zone of feeder dykes are probably caused by mafic material intruded from the feeder dyke zone.

The Oligocene volcano at km 270 (V3 Figs. 3, 9b, 10a) is not underlain by pull-ups in velocity contours in the same way as the Eocene volcano to the west. Note that since BIS-

2008 is located some km south of this volcano (Fig. 3) we are not able to tell if velocity pull-ups exist below the center of the volcano. This volcano, however, is not associated with strong magnetic anomalies (Figs. 8b, 9a). We therefore suggest that the Oligocene volcanic activity was characterized by less intensive feeder dyke systems which did not produce velocity pull-ups and magnetic anomalies similar to the Eocene volcanic center. These small amounts of volcanism were not able to produce regional volcanic flows. Thus, all the Oligocene volcanic products are located close to the eruption centers.

The P-07 profile (Fig. 2) does not show similar high crustal velocities in the crossing point with BIS-2008 (Clark et al. 2009). It is not possible to fit our OBS data using a velocity structure similar to what is presented in Clark et al. (2009). Hence the crustal velocities in the northwestern end of P-07 are probably too low. This is most likely a result of poor ray coverage in the end of the profile.

East of the Oligocene volcano (V3 Fig. 3) crustal velocities decrease rapidly (Figs. 9b, 10a). Early Eocene volcanic flows are observed in the MCS data as far east as CFZ at ~km 315, but these flows are not underlain by high velocity crust and high magnetic anomalies. The basaltic flows in the eastern areas of VVP most likely erupted from the Early Eocene volcanic center (V1 Fig. 3) or from similar volcanoes located on the conjugate margin. This implies that the Early Eocene extrusives have flowed more than 80 km away from the volcano.

The low velocities in the crust east of V3 (Fig. 9b, 10a) imply sedimentary rocks at depths of 10 km or more. Czuba et al. (2011) suggested that this sedimentary basin is delineated by faults both in the west and in the east. The transition from high velocity crust in the northwestern VVP to low velocities in the east, however, is relatively smooth (Figs. 9b, 10a). The western boundary of the sedimentary basin is therefore probably not fault related. Instead we favor an interpretation where the sedimentary basin becomes more and more

intruded from east to west. Much of the high velocity crust in the western parts of VVP may therefore consist of highly intruded sedimentary rocks.

No major changes in crustal structure are observed at CFZ except close to the seabed where higher velocities are observed on the eastern side of the fault (Figs. 9b, 10a). The shallow boreholes (Fig. 2) show that this is because Eocene sediments are located close to the seabed east of the fault while a thick Late Pliocene- Pleistocene package is observed west of the fault (Sættem et al. 1994). CFZ also marks the eastward termination of Early Eocene volcanic flows along BIS-2008. The deep sedimentary basin east of V3 does not change in character at CFZ.

The eastern boundary of the deep sedimentary basin coincides with the Knølegga Fault (Fig. 3). East of km 350, which is the position of the Knølegga Fault, high velocities are located close to the seabed (Figs. 9b, 10a). This is the Stappen High which lacks sedimentary rocks younger than Triassic age (Worsley et al. 2001).

The deep sedimentary basin west of the Knølegga Fault Zone was interpreted by Czuba et al. (2011) as rocks of mainly Permian/Carboniferous age. The bottom of their basin, however, was located at 6 km depth, around 4 km shallower than in our model. We agree with their interpretation in the lower parts of the basin but suggest that most of the basin consists of Mesozoic sedimentary rocks that possibly contain small amounts of mafic sill intrusions. The basin is probably a half graben structure related to movements along the Knølegga Fault as suggested by Jebsen (1998).

5.4 Geological interpretation of the velocity model

Our preferred geological interpretation for BIS-2008 is shown in Fig. 16. The boundary between oceanic layers 2 and 3 is placed at the 6.75 km/s contour in the first arrival tomography model. This contour does fit very well (less than 1 km difference) with the

modeled top oceanic layer 3 boundary in the Rayinvr model. Moho is placed close to the 7.75 km/s contour in the tomography model and the difference between this Moho and the Moho from the Rayinvr model is less than 1 km, except southwest of km 40 where the velocity uncertainty is high (Fig. 10b). The COB is interpreted at km 200 where the distance between the 6 km/s and 7 km/s contours changes resulting in lower velocity gradients towards northeast. Moho depths increase northeast of the COB and the change in crustal architecture is also observed in the strong reduction in Bouguer anomalies (Fig. 9a). The pull-up of velocity contours at ~km 240 coincides with the position of the Early Eocene volcanic center (V1 Fig. 3) and a strong positive magnetic anomaly (Fig. 9a). We interpret the velocity pull-ups as high velocity Early Eocene mafic feeder dykes. High velocities (>6 km/s) at shallow levels until km 275 is interpreted as sedimentary and crystalline rocks intruded by mafic intrusions. It is not possible to conclude if these rocks are heavily intruded sedimentary rocks or less intruded felsic rocks, but the velocity structure farther northeast makes it likely that at least some of these rocks are heavily intruded sedimentary rocks of Mesozoic and possibly Late Paleozoic age. East of km 275 the velocity structure indicates sedimentary rocks at depths of 10 km or more. We have interpreted this area as a major Mesozoic and possibly Late Paleozoic sedimentary basin bounded to the east by the Knølegga Fault. The position of the CFZ is inserted based on observations from MCS data together with a velocity increase in the shallow sedimentary layers at ~km 315 (Figs. 9b, 10a). This fault is interpreted as the eastern boundary of VVP, but volcanic material exists locally also east of this fault. Moho depths and the thickness of the intruded lower crust in the northeastern parts of the profile are not constrained and are therefore marked with question marks. East of the Knølegga Fault we have interpreted crystalline basement rocks below an approximately 1 km thick layer of Late Paleozoic-Early Mesozoic rocks, similar to what is observed on Bear Island (Worsley et al. 2001).

6. Conclusions

Geophysical data show that VVP consists of a western zone with high velocity crust and volcanic constructions, and an eastern part with lower crustal velocities and a lack of volcanic constructions. The high velocities in the crust in the western part are evidence for the presence of mafic intrusions. Below volcano V1 a pull-up of the velocity contours is observed. The strong correlation between this volcano, a strong positive magnetic anomaly and high crustal velocities imply the presence of Early Eocene mafic feeder dykes. Towards the east in VVP the amount of mafic material in the crust decreases. Between volcano V3 and the Knølegga Fault a sedimentary basin province is observed. Here the sedimentary thickness may be more than 10 km. To the east of this basin province the Stappen High, separated from the basin province by the Knølegga Fault, shows high velocities close to the seabed proving the absence of rocks younger than Early Mesozoic.

Our results support an interpretation of a narrow continent-ocean transition zone in VVP, in the area with strongest gradients in the Bouguer anomalies at ~km 200 along BIS-2008. Because of the narrow width of the COT we can classify it as a COB.

The oceanic crust west of the volcanic province is buried by a thick package of low-velocity Cenozoic sedimentary rocks. These low velocities are a result of overpressure in the Bear Island Fan. The igneous oceanic crust shows a two-layered structure consisting of an upper layer with strong vertical velocity gradients and a lower layer with high velocities and low velocity gradients, in accordance with a typical oceanic layer 2 and oceanic layer 3 crustal architecture. The igneous oceanic crust is thicker than the global average close to the COB and thinner below the global average in the southwestern parts of the profile. We suggest

that is the result of elevated mantle temperatures produced along the Senja Fracture Zone by brittle weakening and shear heating prior to the major plate reorganization in Early Oligocene.

Acknowledgements

This work was financed by Vista, the research cooperation between Statoil and The Norwegian Academy of Science and Letters, project number 6253. Data acquisition was funded by the Research Council of Norway as a part of the IPY project “The Dynamic Continental Margin Between the Mid-Atlantic-Ridge System (Mohns Ridge, Knipovich Ridge) and the Bear Island Region” lead by Johannes Schweitzer (NORSAR). We would like to thank the captain and crew on R/V Håkon Mosby. Participants from Hokkaido University are acknowledged for their effort during acquisition and processing of OBS data. Ole Meyer, Helge Johnsen, Aleksander Kandilarov and Alexander Minakov from University of Bergen and Stephen A. Clark from University of Oslo are thanked for their contribution during OBS acquisition. Our Polish colleagues from Polish Academy of Sciences and University of Warsaw fired the TNT shots and acquired the Texan land station data on Bear Island. The group from University of Potsdam acquired the broadband land data on Bear Island and Alfred Wegener Institute was responsible for the broadband OBS data. Arne Gidskehaug processed the gravity data. Comments from Atle Austegard, Berit Hjelstuen, Christian Eide and Trond Kvarven improved the paper. GMT (Wessel and Smith 1998) was used to create many of the figures. Finally we thank the editor, Shu-Kun Hsu, together with Bob White and an anonymous reviewer for constructive feedback on our manuscript.

References

- Barrère C, Ebbing J, Gernigon L (2009) Offshore prolongation of Caledonian structures and basement characterization in the western Barents Sea from geophysical modeling. *Tectonophysics* 470: 71-88. doi: 10.1016/j.tecto.2008.07.012
- Barrère C, Ebbing J, Gernigon L (2011) 3-D density and magnetic crustal characterization of the southwestern Barents Shelf: implications for the offshore prolongation of the Norwegian Caledonides. *Geophys J Int* 184: 1147-1166. doi: 10.1111/j.1365-246X.2010.04888.x
- Bauer K, Trumbull RB, Vietor T (2003) Geophysical images and a crustal model of intrusive structures beneath the Messum ring complex, Namibia. *Earth Planet Sci Lett* 216: 65-80. doi: 10.1016/S0012-821X(03)00486-2
- Behn MD, Boettcher MS, Hirth G (2007) Thermal structure of oceanic transform faults. *Geology* 35: 307-310
- Bown JW, White RS (1994) Variation with spreading rate of oceanic crustal thickness and geochemistry. *Earth Planet. Sci. Lett.* 121: 435-449
- Breivik AJ, Faleide JJ, Gudlaugsson ST (1998) Southwestern Barents Sea margin: late Mesozoic sedimentary basins and crustal extension. *Tectonophysics* 293: 21-44
- Breivik AJ, Mjelde R, Grogan P, Shimamura H, Murai Y, Nishimura Y (2003) Crustal structure and transform margin development south of Svalbard based on ocean bottom seismometer data. *Tectonophysics* 369: 37-70. doi: 10.1016/S0040-1951(03)00131-8
- Breivik AJ, Mjelde R, Grogan P, Shimamura H, Murai Y, Nishimura Y (2005) Caledonide development offshore-onshore Svalbard based on ocean bottom seismometer, conventional seismic, and potential field data. *Tectonophysics* 401: 79-117. doi: 10.1016/j.tecto.2005.03.009

- Breivik AJ, Verhoef J, Faleide JI (1999) Effect of thermal contrasts on gravity modeling at passive margins: Results from the western Barents Sea. *J Geophys Res* 104: 15293-15311
- Cande SC, Kent DV (1995) Revised calibration of the geomagnetic polarity timescale for the Late Cretaceous and Cenozoic. *J Geophys Res* 100: 6093-6095
- Christensen NI, Mooney WD (1995) Seismic velocity structure and composition of the continental crust: A global view. *J Geophys Res* 100: 9761-9788
- Clark SA, Faleide JI, Ritzmann O, Mjelde R (2009) Multi-stage rift evolution of the SW Barents Sea from wide-angle seismic velocity modeling. *Geophys Res Abs* 11: 12599
- Czuba W, Grad M, Mjelde R, Guterch A, Libak A, Krüger F, Murai Y, Schweitzer J and the IPY Project Group (2011) Continent-ocean-transition across a trans-tensional margin segment: off Bear Island, Barents Sea. *Geophys J Int* 184: 541-554. doi: 10.1111/j.1365-246X.2010.04873.x
- Dimakis P, Braathen BI, Faleide JI, Elverhøi A, Gudlaugsson ST (1998) Cenozoic erosion and the preglacial uplift of the Svalbard-Barents Sea region. *Tectonophysics* 300: 311-327
- Døssing A, Dahl-Jensen T, Thybo H, Mjelde R, Nishimura Y (2008) East Greenland Ridge in the North Atlantic Ocean: An integrated geophysical study of a continental sliver in a boundary transform setting. *J Geophys Res* 113: B10107. doi: 10.1029/2007JB005536
- Eidvin T, Goll RM, Grogan P, Smelror M, Ulleberg K (1998) The Pleistocene to Middle Eocene stratigraphy and geological evolution of the western Barents Sea continental margin at well site 7316/5-1 (Bjørnøya West area). *Norwegian J Geol* 78: 99-123
- Eldholm O, Faleide JI, Myhre AM (1987) Continent-ocean transition at the western Barents Sea/Svalbard continental margin. *Geology* 15: 1118-1122

- Eldholm O, Sundvor E, Vogt PR, Hjelstuen BO, Crane K, Nilsen AK, Gladchenko TP (1999) SW Barents Sea continental margin heat flow and Håkon Mosby Mud Volcano. *Geo-Marine Lett* 19: 29-37
- Engen Ø, Faleide JI, Dyreng TK (2008) Opening of the Fram Strait gateway: A review of plate tectonic constraints. *Tectonophysics* 450: 51-69. doi:10.1016/j.tecto.2008.01.002
- Faleide JI, Gudlaugsson ST, Eldholm O, Myhre AM, Jackson HR (1991) Deep seismic transects across the sheared western Barents Sea-Svalbard continental margin. *Tectonophysics* 189: 73-89
- Faleide JI, Myhre AM, Eldholm O (1988) Early Tertiary volcanism at the western Barents Sea margin. In: Morton AC, Parson LM (eds) *Early Tertiary Volcanism and the Opening of the NE Atlantic*. Geol Soc Special Publication 39, pp 135-146
- Faleide JI, Solheim A, Fiedler A, Hjelstuen BO, Andersen ES, Vanneste K (1996) Late Cenozoic evolution of the western Barents Sea-Svalbard continental margin. *Global Planet Change* 12: 53-74
- Faleide JI, Tsikalas F, Breivik AJ, Mjelde R, Ritzmann O, Engen Ø, Wilson J, Eldholm O (2008) Structure and evolution of the continental margin off Norway and the Barents Sea. *Episodes* 31: 82-91
- Faleide JI, Vågnes E, Gudlaugsson ST (1993). Late Mesozoic-Cenozoic evolution of the south-western Barents Sea in a regional rift-shear tectonic setting. *Mar Pet Geol* 10: 186-214
- Fiedler A, Faleide JI (1996) Cenozoic sedimentation along the southwestern Barents Sea margin in relation to uplift and erosion of the shelf. *Global Planet Change* 12: 75-93
- Gabrielsen RH, Færseth RB, Jensen LN, Kalheim JE, Riis F (1990) Structural elements of the Norwegian continental shelf. Part I: The Barents Sea Region. *NPD-Bulletin* 6: 1-33

- Hinz K, Eldholm O, Block M, Skogseid J (1993) Evolution of North Atlantic volcanic continental margins. In: Parker JR (ed) Petroleum Geology of Northwest Europe: Proceedings of the 4th Conference. The Geological Soc, London, pp 901-913
- Hjelstuen BO, Elverhøi A, Faleide JJ (1996) Cenozoic erosion and sediment yield in the drainage area of the Storfjorden Fan. *Global Planet Change* 12: 95-117
- Håkansson E, Pedersen SAC (2001) The Wandel Hav Strike-Slip Mobile Belt – A Mesozoic plate boundary in North Greenland. *Bull Geol Soc Denmark* 48: 149-158
- Jackson HR, Faleide JJ, Eldholm O (1990) Crustal Structure of the Sheared Southwestern Barents Sea Continental Margin. *Mar Geol* 93: 119-146
- Jakobsson M, Backman J, Rudels B, Nycander J, Frank M, Mayer L, Jokat W, Sangiorgi F, O'Regan M, Brinkhuis H, King J, Moran K (2007) The Early Miocene onset of a ventilated circulation regime in the Arctic Ocean. *Nature* 447: 986-990. doi: 10.1038/nature05924
- Jakobsson M, Macnab R, Mayer L, Anderson R, Edwards M, Hatzky J, Schenke HW, Johnson P (2008) An improved bathymetric portrayal of the Arctic Ocean: Implications for ocean modeling and geological, geophysical and oceanographic analyses. *Geophys Res Lett* 35: L07602. doi: 10.1029/2008GL033520
- Jebsen C (1998) Kenozoisk utvikling av Vestbakkvulkanittprovinsen på den vestlige Barentshavsmarginen. Cand. Scient. Thesis, University of Oslo
- Kandilarov A, Landa H, Mjelde R, Pedersen RB, Okino K, Murai Y (2010) Crustal structure of the ultra-slow spreading Knipovich Ridge, North Atlantic, along a presumed ridge segment center. *Mar Geophys Res* 31: 173-195. doi: 10.1007/s11001-010-9095-8
- Klingelhöfer F, Géli L, Matias L, Steinsland N, Mohr J (2000) Crustal structure of a super-slow spreading centre: a seismic refraction study of Mohns Ridge, 72°N. *Geophys J Int* 141: 509-526

- Knutsen SM, Larsen KI (1997) The late Mesozoic and Cenozoic evolution of the Sørvestsnaget Basin: A tectonostratigraphic mirror for regional events along the Southwestern Barents Sea Margin?. *Mar Pet Geol* 14: 27-54
- Korenaga J, Holbrook WS, Kent GM, Kelemen PB, Detrick RS, Larsen HC, Hopper JR, Dahl-Jensen T (2000) Crustal structure of the southeast Greenland margin from joint refraction and reflection seismic tomography. *J Geophys Res* 105: 21591-21614
- Libak A, Eide CH, Mjelde R, Keers H, Flüh E (2012) From pull-apart basins to ultraslow spreading: Results from the western Barents Sea margin. *Tectonophysics* 514-517: 44-61
- Lorenzo JM (1997) Sheared continent-ocean margins: an overview. *Geo-Marine Lett* 17: 1-3.
- Maus S, Sazonova T, Hemant K, Fairhead JD, Ravat D (2007) National Geophysical Data Center candidate for the World Digital Magnetic Anomaly Map. *Geochem Geophys Geosystems* 8, Q06017. doi: 10.1029/2007GC001643
- Minakov A (2011) Structure and evolution of the northern Barents Sea-Lomonosov Ridge margins from a multidisciplinary geophysical approach. Dissertation, University of Bergen
- Minshull TA (2009) Geophysical characterization of ocean-continent transition at magma-poor rifted margins. *C. R. Geoscience* 341: 382-393. doi: 10.1016/j.crte.2008.09.003
- Minshull TA, Muller MR, Robinson CJ, White RS, Bickle MJ (1998) Is the oceanic Moho a serpentinization front?. In: Mills RA, Harrison K (eds) *Modern Ocean Floor Processes and the Geological Record*. Geological Society, London, Special Publications 148, pp 71-80
- Minshull TA, Muller MR, White RS (2006) Crustal structure of the Southwest Indian Ridge at 66°E: seismic constraints. *Geophys J Int* 166: 135-147. doi: 10.1111/j.1365-246X.2006.03001.x

- Mjelde R, Breivik AJ, Elstad H, Ryseth, AE, Skilbrei JR, Opsal JG, Shimamura H, Murai Y, Nishimura Y (2002) Geological development of the Sørvestnaget Basin, SW Barents Sea, from ocean bottom seismic, surface seismic and potential field data. *Norwegian J Geol* 82: 183-202
- Mjelde R, Faleide JI (2009) Variation of Icelandic and Hawaiian magmatism: evidence for co-pulsation of mantle plumes? *Mar Geophys Res* 30: 61-72
- Mjelde R, Breivik AJ, Raum T, Mittelstaedt E, Ito G, Faleide JI (2008) Magmatic and tectonic evolution of the North Atlantic. *Journal of the Geological Society* 165: 31-42
- Myhre AM, Eldholm O, Sundvor E (1982) The margin between Senja and Spitsbergen Fracture Zones: Implications from plate tectonics. *Tectonophysics* 89: 33-50
- Parkin CJ, Lunnon ZC, White RS, Christie PAF and iSIMM Team (2007) Imaging the pulsing Iceland mantle plume through the Eocene. *Geology* 35: 93-96
- Richardsen G, Henriksen E, Vorren TO (1991) Evolution of the Cenozoic sedimentary wedge during rifting and sea-floor spreading west of the Stappen High, western Barents Sea. *Mar Geol* 101: 11-30
- Ritzmann O, Faleide JI (2007) Caledonian basement of the western Barents Sea. *Tectonics* 26, TC5014. doi: 10.1029/2006TC002059
- Ryseth A, Augustson JH, Charnock M, Haugerud O, Knutsen S-M, Midtbøe PS, Opsal JG, Sundsbø G (2003) Cenozoic stratigraphy and evolution of the Sørvestsnaget Basin, southwestern Barents Sea. *Norwegian J Geol* 83: 107-130
- Scott CL, Shillington DJ, Minshull TA, Edwards RA, Brown PJ, White NJ (2009) Wide-angle seismic data reveal extensive overpressures in the Eastern Black Sea Basin. *Geophys J Int* 178: 1145-1163. doi: 10.1111/j.1365-246X.2009.04215.x
- Scrutton RA (1979) On sheared passive continental margins. *Tectonophysics* 59: 293-305.

- Smith MP (2000) Cambro-Ordovician stratigraphy of Bjørnøya and North Greenland: constraints on tectonic models for the Arctic Caledonides and the Tertiary opening of the Greenland Sea. *Journal of Geological Society* 157: 459-470
- Sættem J, Bugge T, Fanavoll S, Goll RM, Mørk A, Mørk MBE, Smelror M, Verdenius JG (1994) Cenozoic margin development and erosion of the Barents Sea: Core evidence from southwest of Bjørnøya. *Mar Geol* 118: 257-281
- Wessel P, Smith WHF (1998) New, improved version of generic mapping tools released. *EOS Trans AGU* 79: 579-579
- White RS, McKenzie D, O'Nions RK (1992) Oceanic Crustal Thickness From Seismic Measurements and Rare Earth Element Inversions. *J Geophys Res* 97: 19683-19715
- Worsley D, Agdestein T, Gjelberg JG, Kirkemo K, Mørk A, Nilsson I, Olaussen S, Steel RJ, Stemmerik L (2001) The geological evolution of Bjørnøya, Arctic Norway: implications for the Barents Shelf. *Norwegian J Geol* 81: 195-234
- Zelt CA (1999) Modelling strategies and model assessment for wide-angle seismic traveltime data. *Geophys J Int* 139: 183-204
- Zelt CA, Barton PJ (1998) Three-dimensional seismic refraction tomography: A comparison of two methods applied to data from the Faeroe Basin. *J Geophys Res* 103: 7187-7210
- Zelt CA, Forsyth DA (1994) Modeling wide-angle seismic data for crustal structure: Southeastern Grenville Province. *J Geophys Res* 99: 11687-11704
- Zelt CA, Smith RB (1992) Seismic traveltime inversion for 2-D crustal velocity structure. *Geophys J Int* 108: 16-34
- Zhang J, Toksöz MN (1998) Nonlinear refraction traveltime tomography. *Geophysics* 63: 1726-1737

Table captions

Table 1 Abbreviations used for seismic phases

Table 2 Statistics for traced rays and calculated travel times for the final Rayinvr velocity model

Figure Captions

Fig. 1 Bathymetry in the Norwegian-Greenland Sea and surrounding continental margins (Jakobsson et al. 2008). Red frame shows the study area (Fig. 2) and black frame shows outline of Fig. 3. Blue circle shows position of the Skrugard prospect where a large oil discovery was made in 2011. Position of the continent-ocean boundary (COB) is from Engen et al. (2008). On the Greenland side a double COB means that the position is uncertain and that it can be located anywhere in between. BF, Bear Island Fan; BI, Bear Island; EGR, East Greenland Ridge; FS, Fram Strait; HR, Hovgård Ridge; SF, Storfjorden Fan; SP, Svalbard Platform; VVP, Vestbakken Volcanic Province; WS, Wandel Sea; YP, Yermak Plateau

Fig. 2 Seismic- and well data used in this study. Red lines represent OBS profiles. MCS profiles are shown as cyan (NPD-77), yellow (NPD-86) and purple (NPD-96) lines. Green lines mark MCS lines shown in this paper. Blue diamond shows location of deep exploration well 7316/5-1 (Eidvin et al. 1998; Knutsen and Larsen 1997) and pink diamonds show the locations of shallow stratigraphic wells (Sættem et al. 1994). Yellow circles represent OBS positions along BIS-2008, green circle represents position of broadband OBS and purple circles represent land stations. Continent-ocean boundary (COB) from Breivik et al. (1999)

and magnetic anomalies (stippled orange lines) are from Engen et al. (2008). Structural elements are from Ritzmann and Faleide (2007). KFZ, Knølegga Fault Zone

Fig. 3 Structural map of Vestbakken Volcanic Province. Gray area shows a rough outline of the province (basaltic flows). The northern extent of the flows are not mapped and are therefore marked with question marks. Location of faults from Sættem et al. (1994) and Jebsen (1998). Locations of volcanoes (named V1-V3) are partly our own interpretations and partly from Jebsen (1998). Position of the Knølegga Fault (KFZ) from Ritzmann and Faleide (2007) is also shown. Continent-ocean boundary (COB) from Breivik et al. (1999). The northeastern parts of BIS-2008 are indicated by blue line and OBS positions are shown as yellow circles. CFZ, Central Fault Zone

Fig. 4 a) The eastern parts of MCS line 5-96. b) MCS line 5-96 with interpretations. Black circles are the projected positions of the OBSs along BIS-2008 onto the MCS lines. Location of the profile is shown in Fig. 2

Fig. 5 a) Data recorded on OBS 5 (Fig. 2). b) Travel times of first arrivals (blue), top oceanic basement reflections (red) and PmP (pink) calculated at OBS 5 using the final Rayinrv velocity model (Fig. 9b)

Fig. 6 a) Data recorded on OBS 9 (Fig. 2). b) Travel times of first arrivals (blue), top basalt reflections (red) and PmP (pink) calculated at OBS 9 using the final Rayinrv velocity model (Fig. 9b)

Fig. 7 a) Data recorded on OBS 13 (Fig. 2). b) Travel times of first arrivals (blue), top basalt? (red) and PmP (pink) calculated at OBS 13 using the final Rayinvr velocity model (Fig. 9b)

Fig. 8 a) Bouguer anomalies (Minakov 2011) and b) Total magnetic intensity anomalies (Maus et al. 2007) for the same area as in Fig. 2. Black line shows location of the spreading center. Structural elements are same as in Fig. 2

Fig. 9 a) Bouguer anomalies (blue) and magnetic anomalies (red) along BIS-2008 (Fig. 2). b) Final Rayinvr velocity model for BIS-2008. Red line segments are constrained by reflections. Layer velocities are numbered at regular intervals. V1 and V3 are volcanoes observed in the MCS data. c) Ray hits in the final velocity model

Fig. 10 a) Velocity model for BIS-2008 obtained using first arrival seismic tomography. The model shown is the average of 200 models obtained by using different initial models. V1 and V3 mark positions of volcanoes. Contour interval is 1 km/s. b) Standard deviation of the velocities shown in a). Contour interval is 0.05 km/s

Fig. 11 a) Observed seismogram for OBS 9. The data are bandpass-filtered and plotted with 8 km/s reduced travel time scale. The data are also scaled by \sqrt{t} in order to convert from 3D to 2D. b) Synthetic seismogram for OBS 9 plotted with 8 km/s reduced travel time scale

Fig. 12 Checkerboard test for the tomography. a) Initial model used in the checkerboard test. b) Perturbed model used to generate synthetic travel times. c) Result of the checkerboard test after 15 iterations with the same correlation lengths as used in the real data inversions

Fig. 13 a) Difference between the Tomo2d model (Fig. 10a) and the Rayinvr model (Fig 9a). Black colors represent areas where the Rayinvr model has velocities more than 0.3 km/s higher than the Tomo2d model and white colors represent areas where the Tomo2d model has velocities more than 0.3 km/s higher than the Rayinvr model. Each color spans an interval of 0.05 km/s

Fig. 14 a) Total igneous thickness (red line), thickness of oceanic layer 2 (blue line) and oceanic layer 3 (green line) for the southwestern 200 km of the BIS-2008 Rayinvr model. b) Average velocities in oceanic layer 2 (blue line) and oceanic layer 3 (green line) along the same segment of the BIS-2008 Rayinvr model as in Fig. 14a

Fig. 15 a) Part of MCS line HB 3-96 located in the continent-ocean transition zone (Fig. 2). b) Part of MCS line 7330-77 located in the continent-ocean transition zone (Fig. 2). c) and d) show geological interpretations of a) and b) respectively. OB, oceanic basement; IS, intruded sediments capped by lava flows

Fig. 16 Preferred geological model. Question marks show uncertain interpretations. CFZ, Central Fault Zone; COB, continent-ocean boundary; KF, Knølegga Fault

Table 1

Abbreviation	Explanation
Px	Refracted in sedimentary rocks
PgP	Reflected from top basalt
Pg1	Refracted in oceanic basement/volcanic section
Pg2P	Reflection in continental crust
Pg2	Refracted from continental crust
Pg3	Refracted from lower crustal layer
Pn	Refracted from upper mantle
PmP	Reflected from Moho/lower crust

Table 2

Phase	Number of picks	Picks traced (%)	RMS (ms)	Normalized Chi-Squared
P _x	1018	97.2	46	0.81
PgP	406	96.1	82	1.33
Pg1	866	97.2	60	0.57
Pg2P	27	92.6	102	1.58
Pg2	892	98.9	85	0.79
Pg3	1920	97.9	82	0.62
Pn	1208	96.8	96	0.70
PmP	231	93.9	260	3.10
Total	6568	97.4	91	0.81

Figure 1
[Click here to download high resolution image](#)

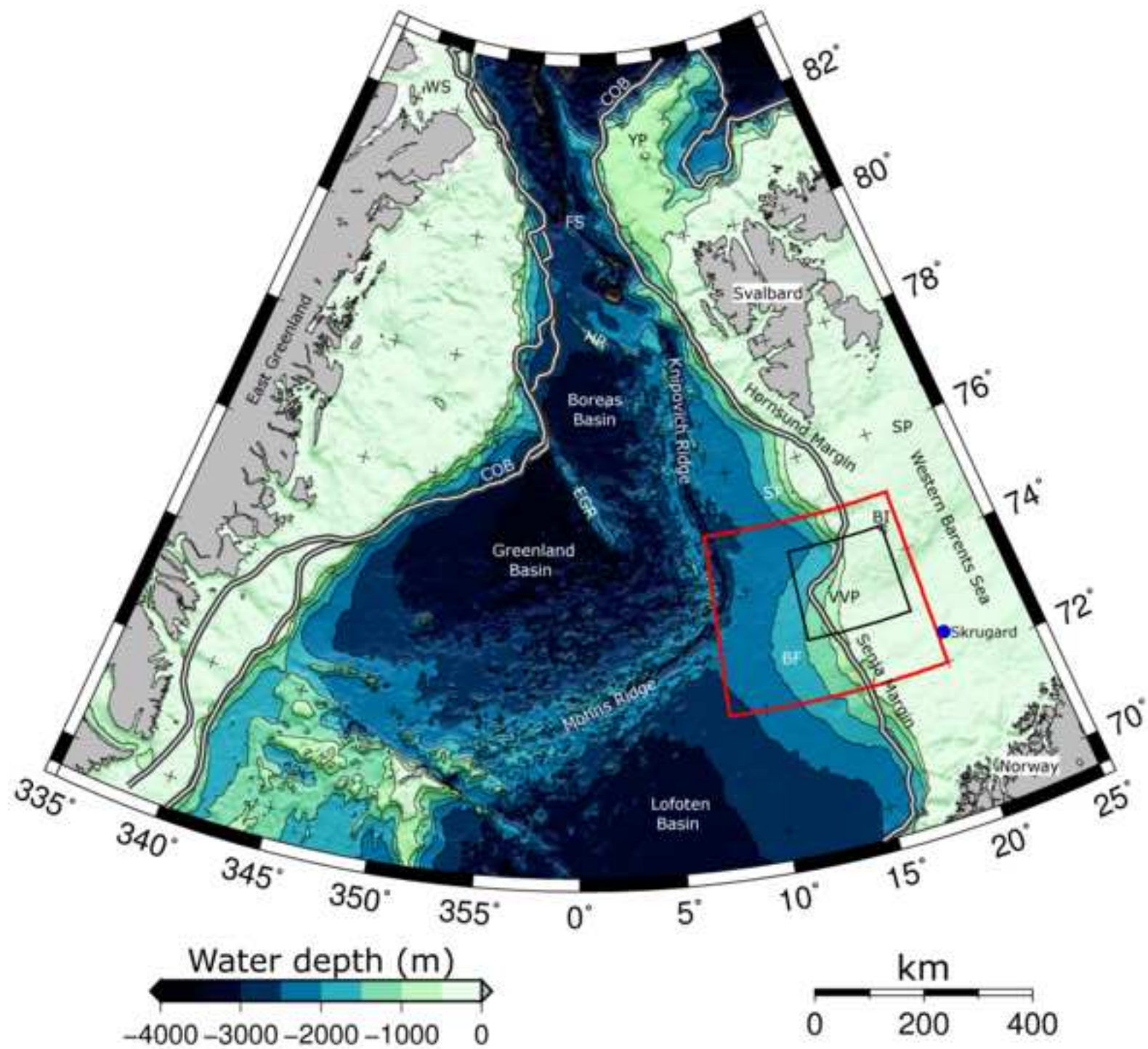


Figure 2
[Click here to download high resolution image](#)

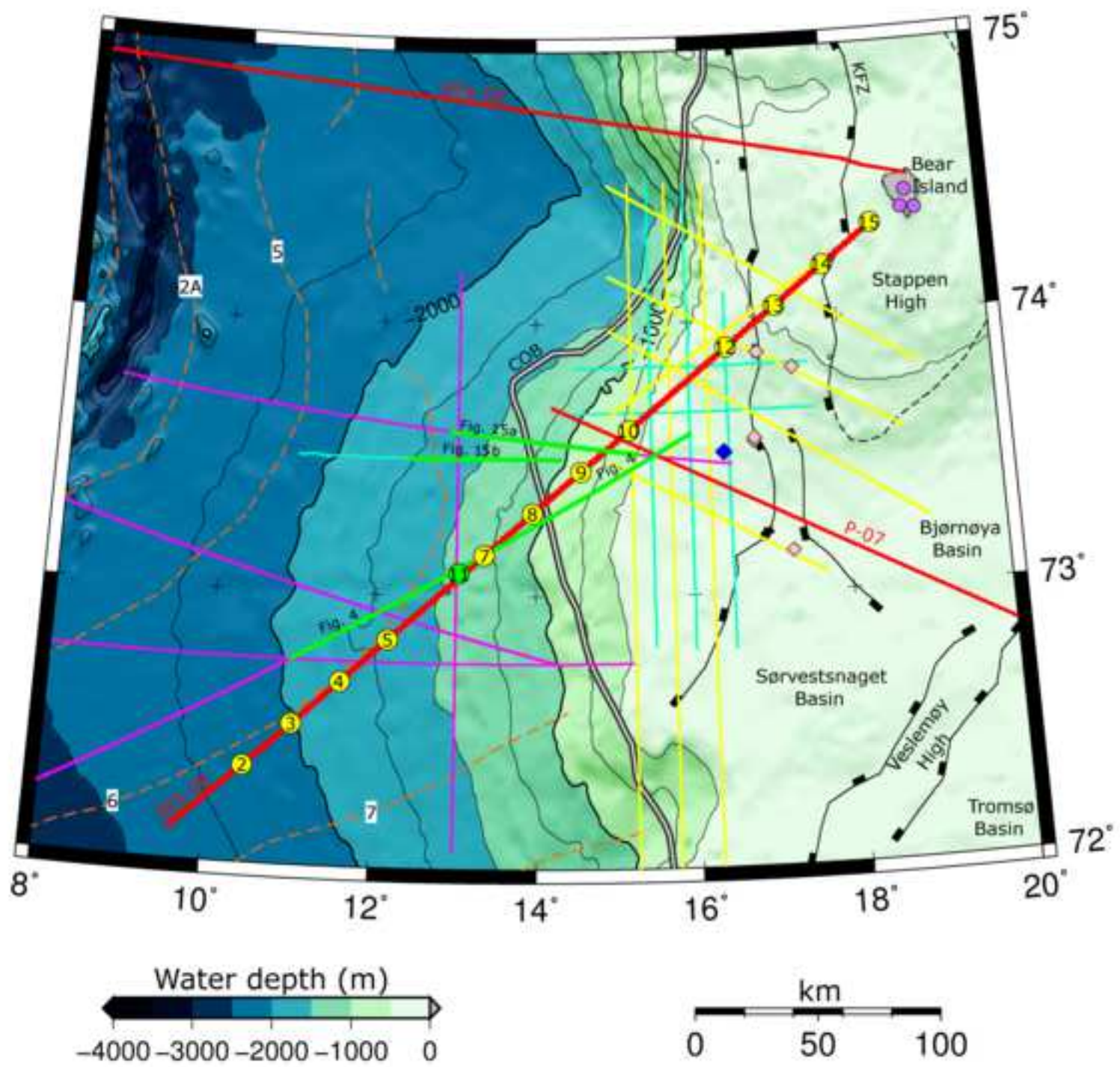


Figure 3
[Click here to download high resolution image](#)

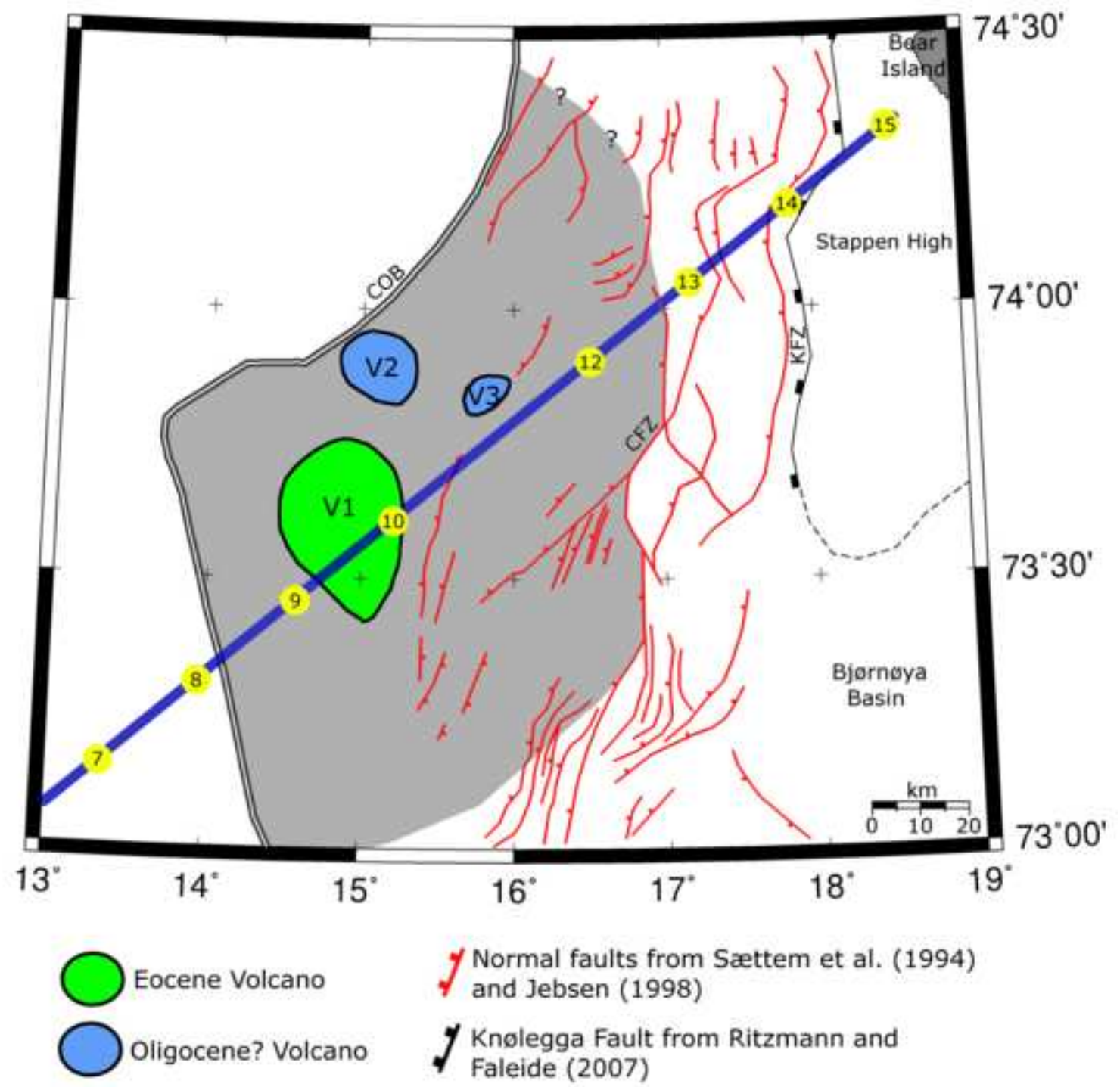


Figure 4

[Click here to download high resolution image](#)

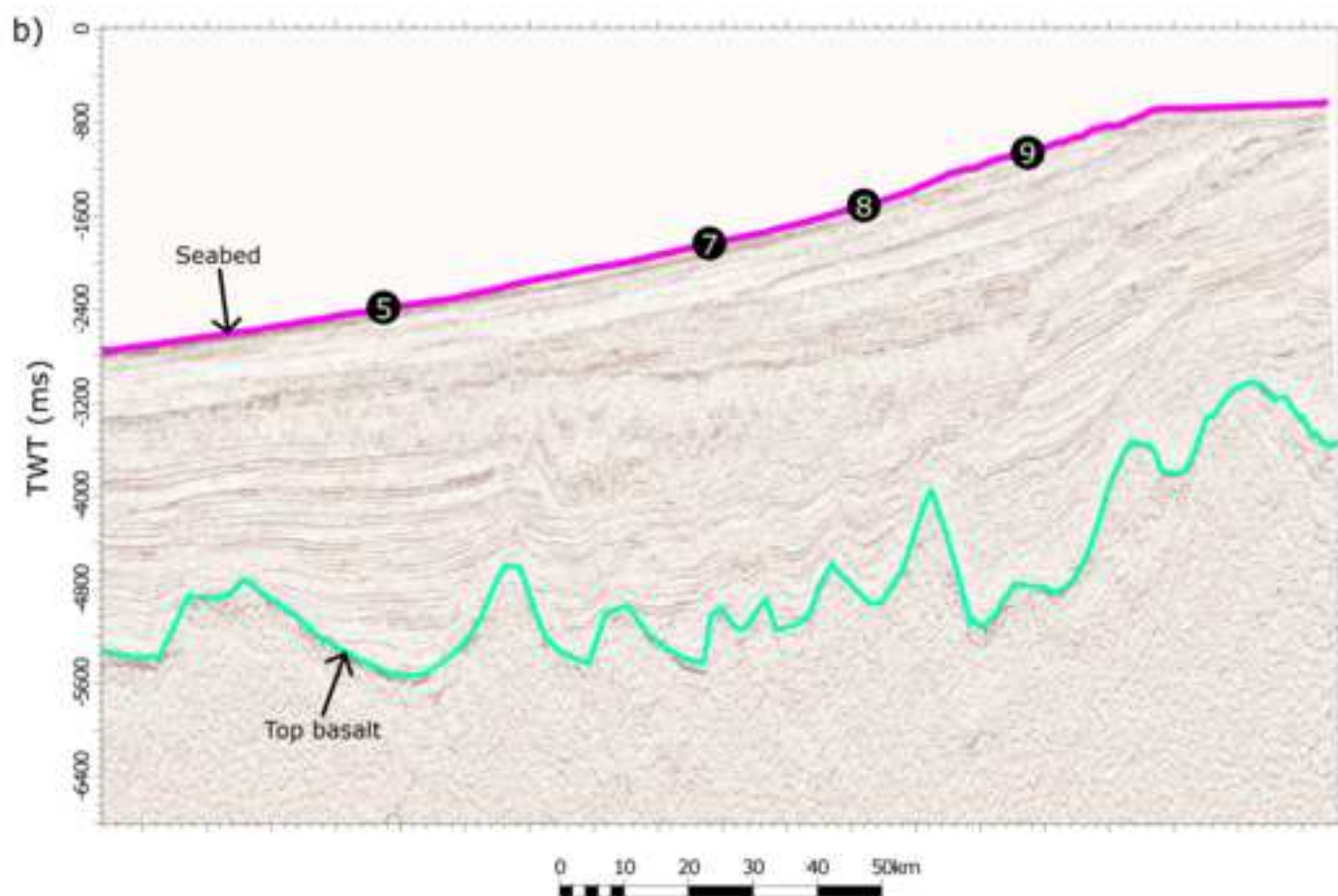


Figure 5
[Click here to download high resolution image](#)

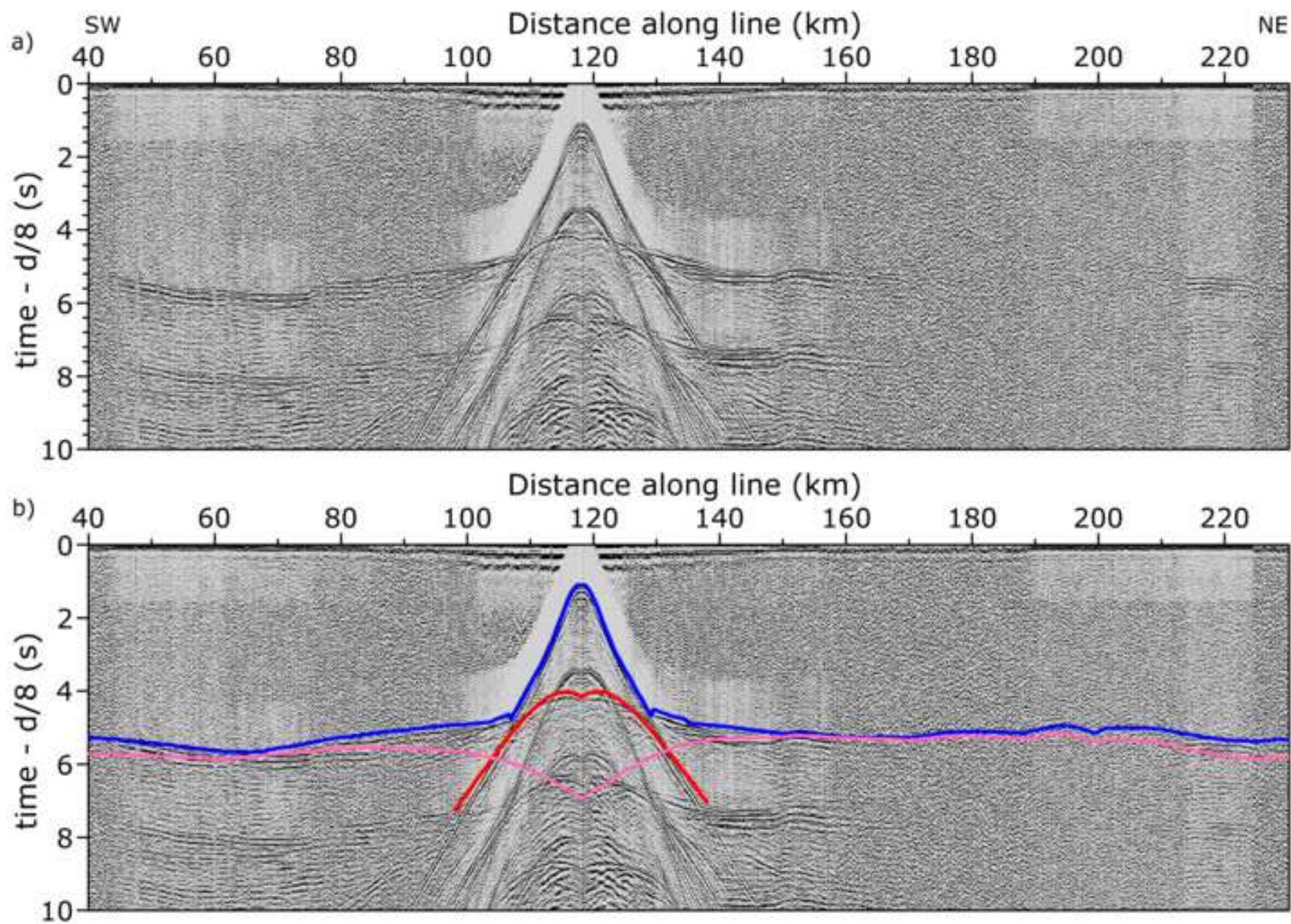


Figure 6
[Click here to download high resolution image](#)

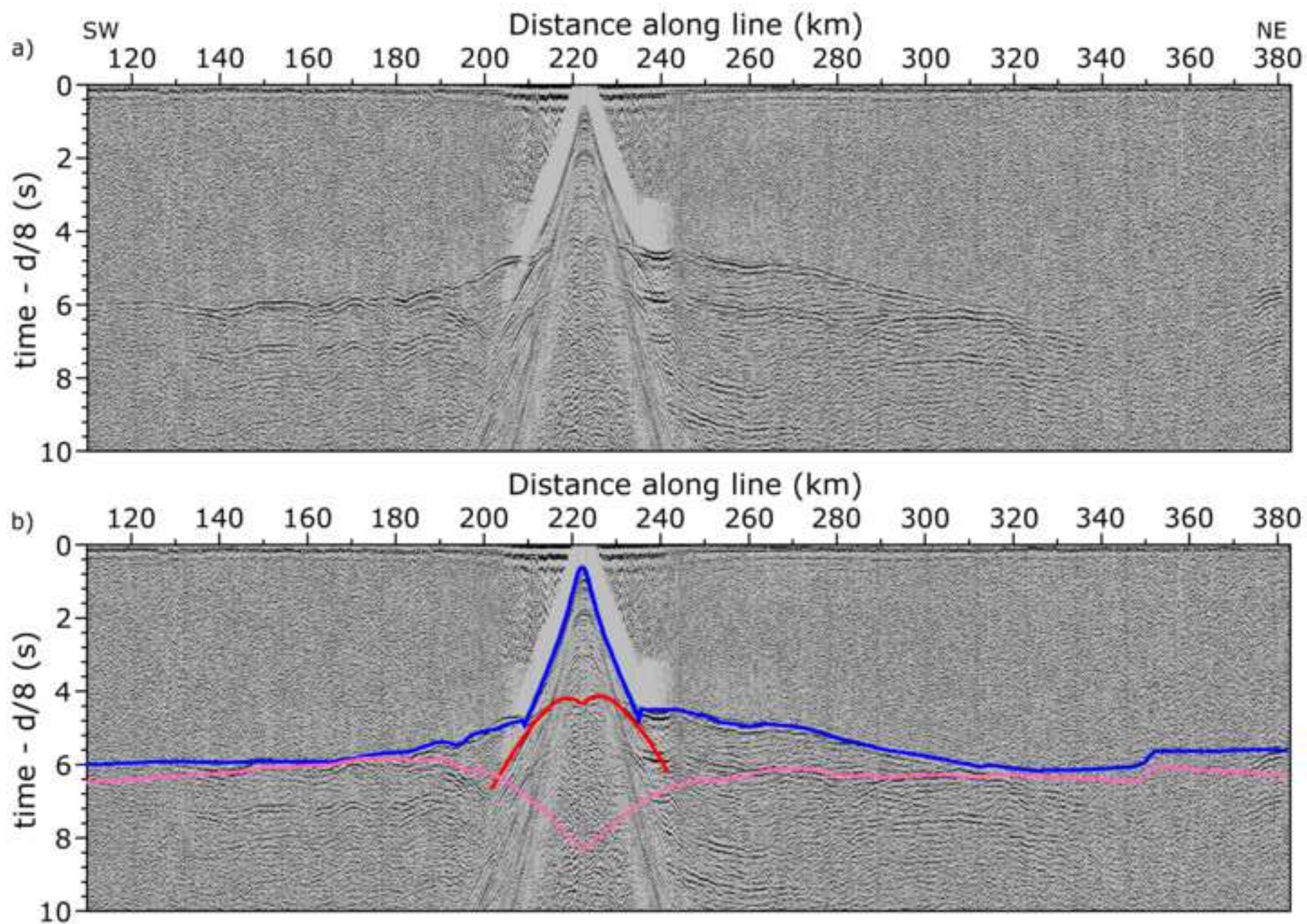


Figure 7
[Click here to download high resolution image](#)

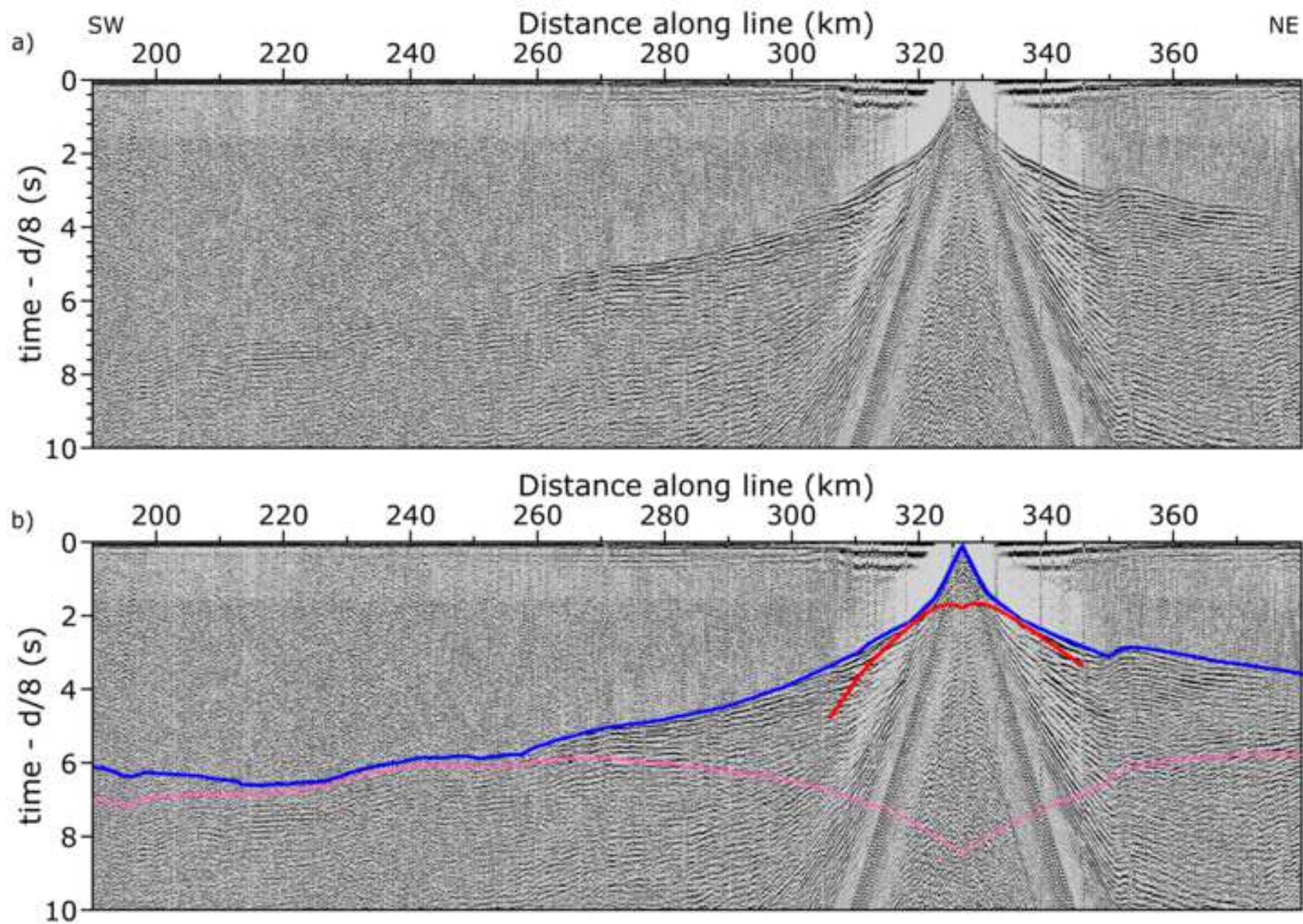


Figure 8
[Click here to download high resolution image](#)

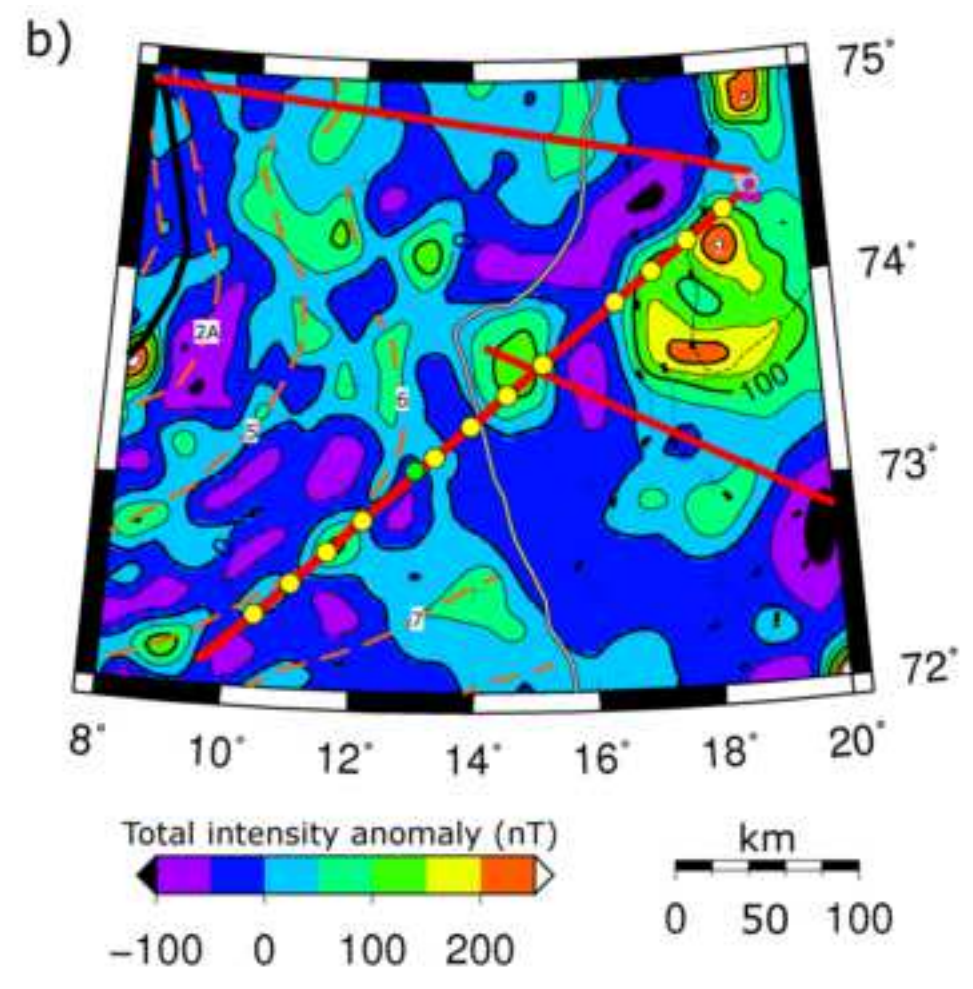
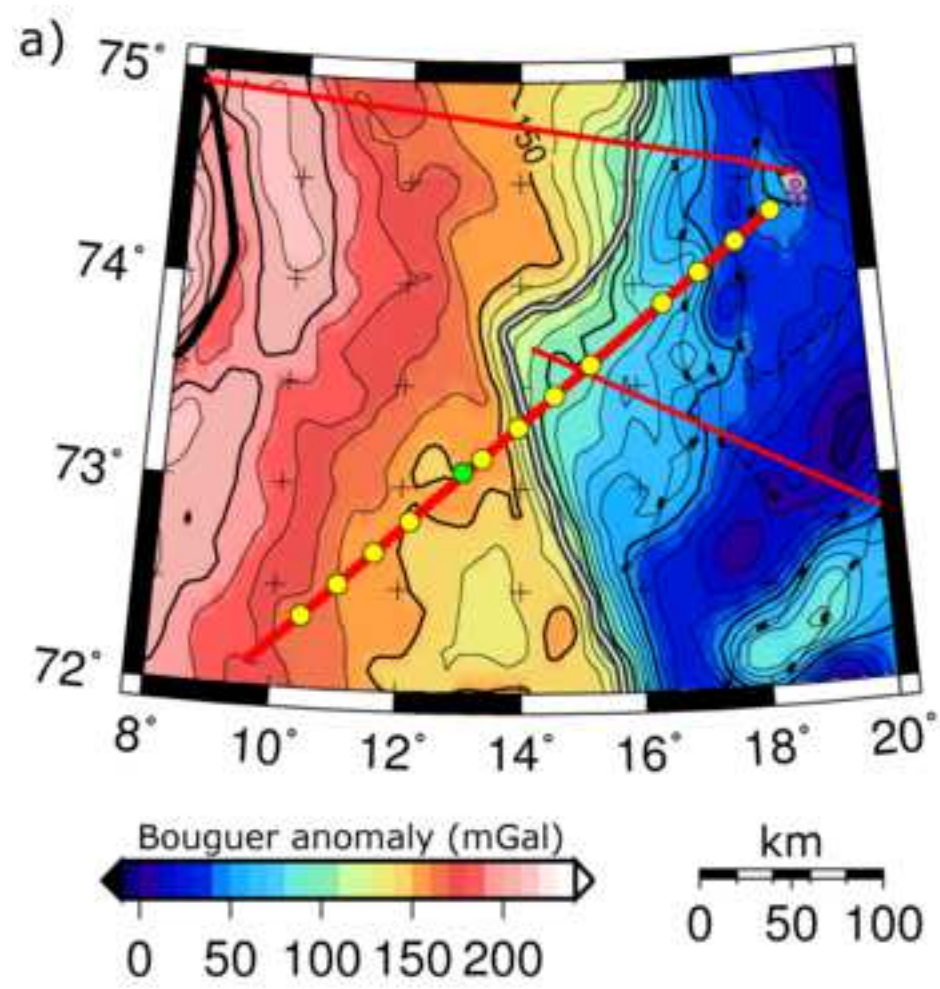


Figure 9
[Click here to download high resolution image](#)

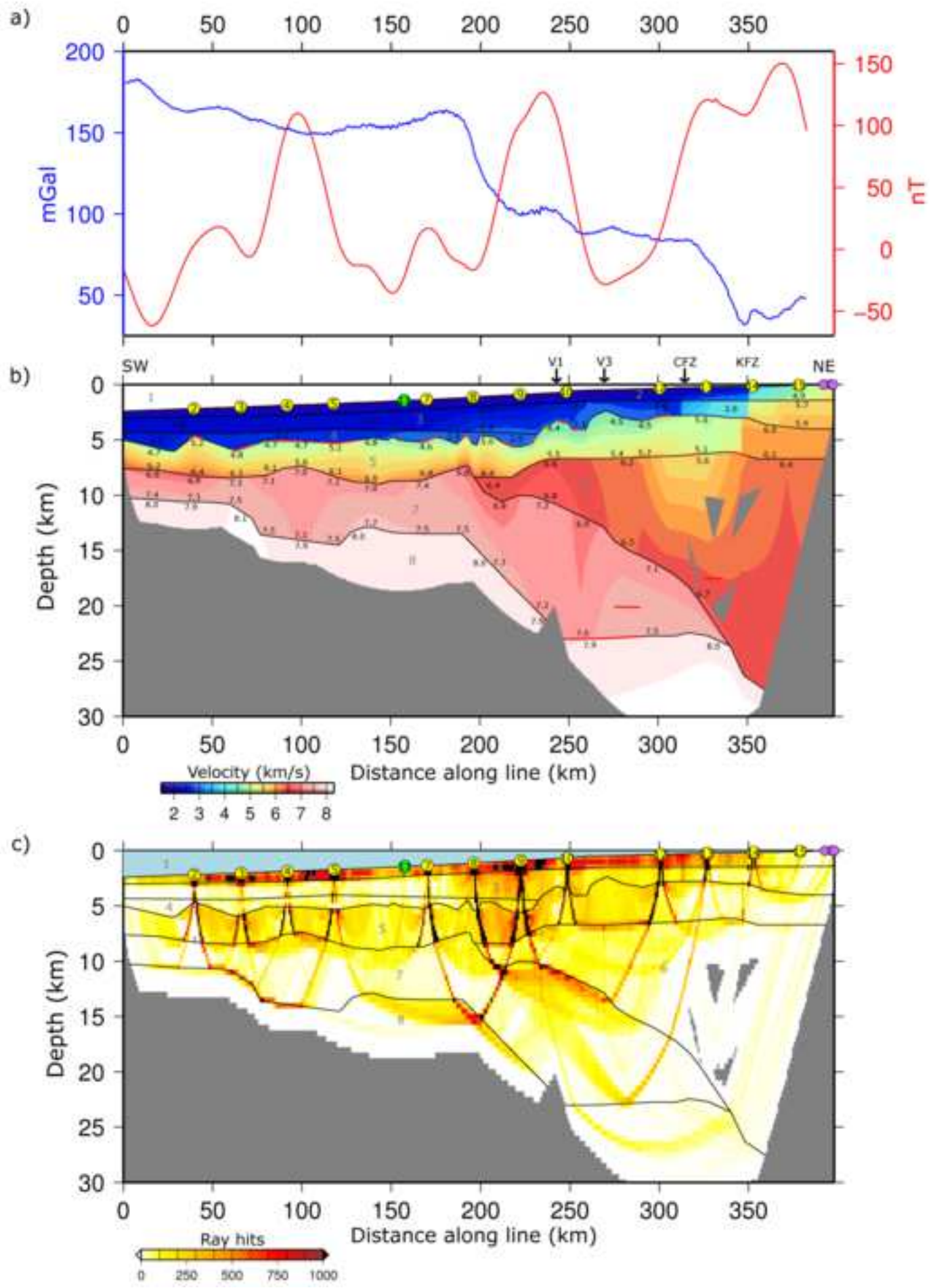


Figure 10
[Click here to download high resolution image](#)

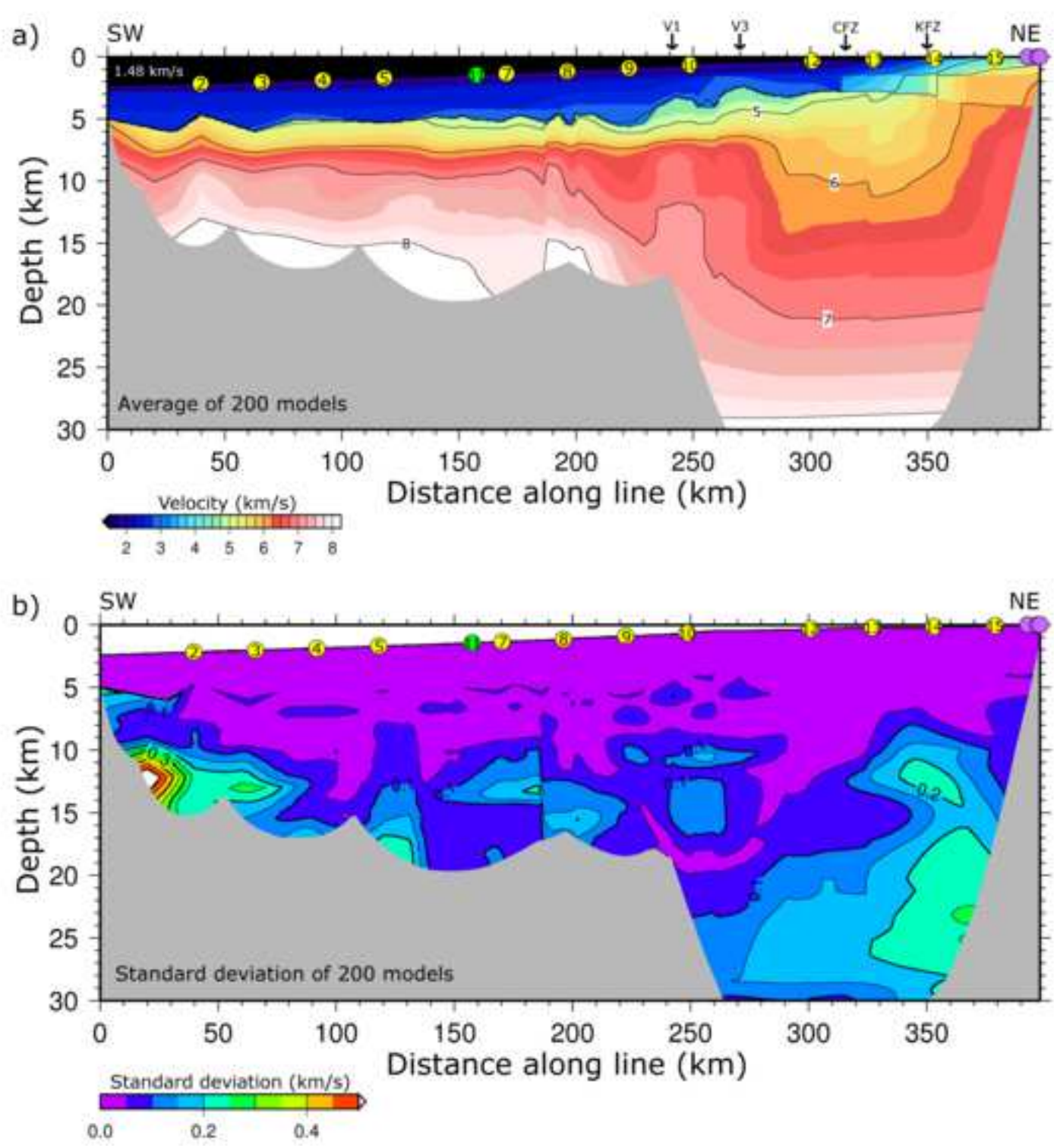


Figure 11
[Click here to download high resolution image](#)

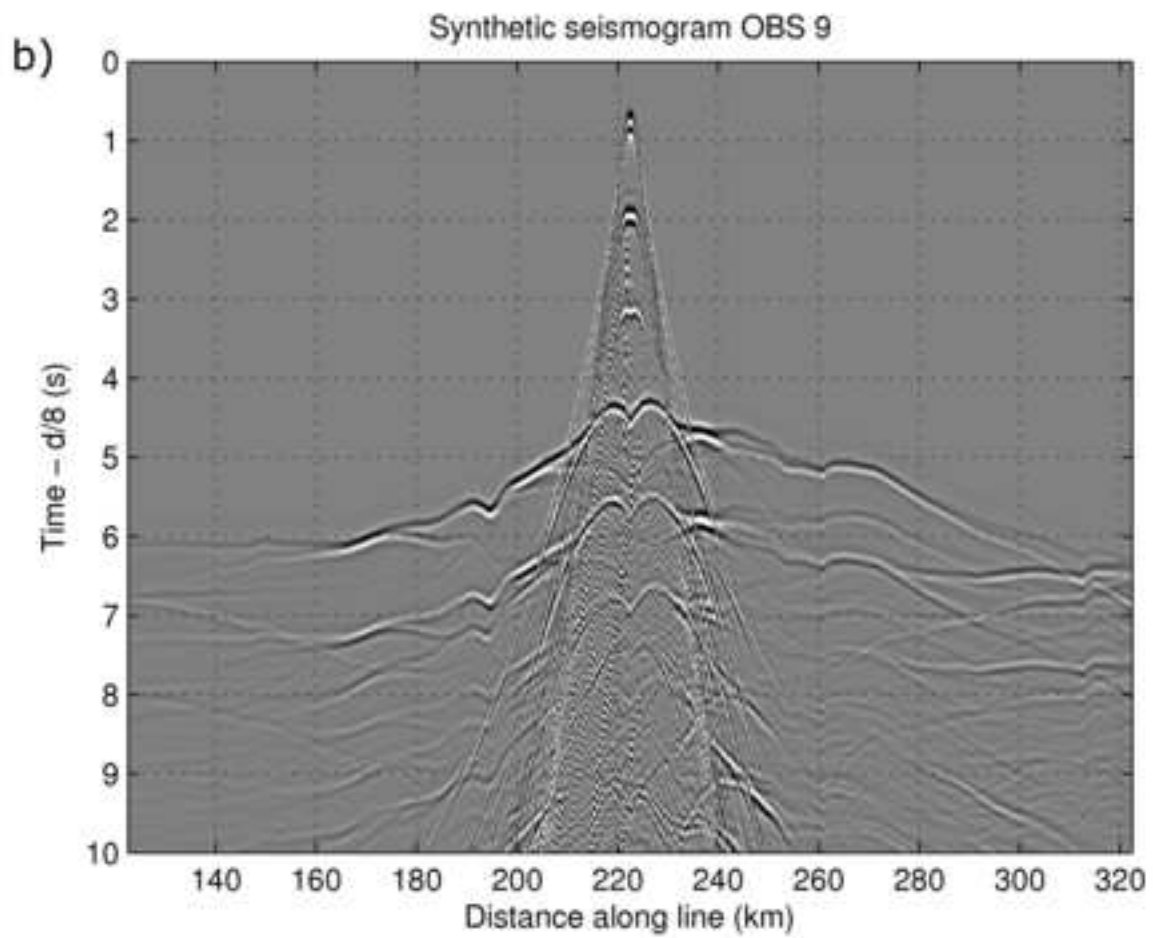
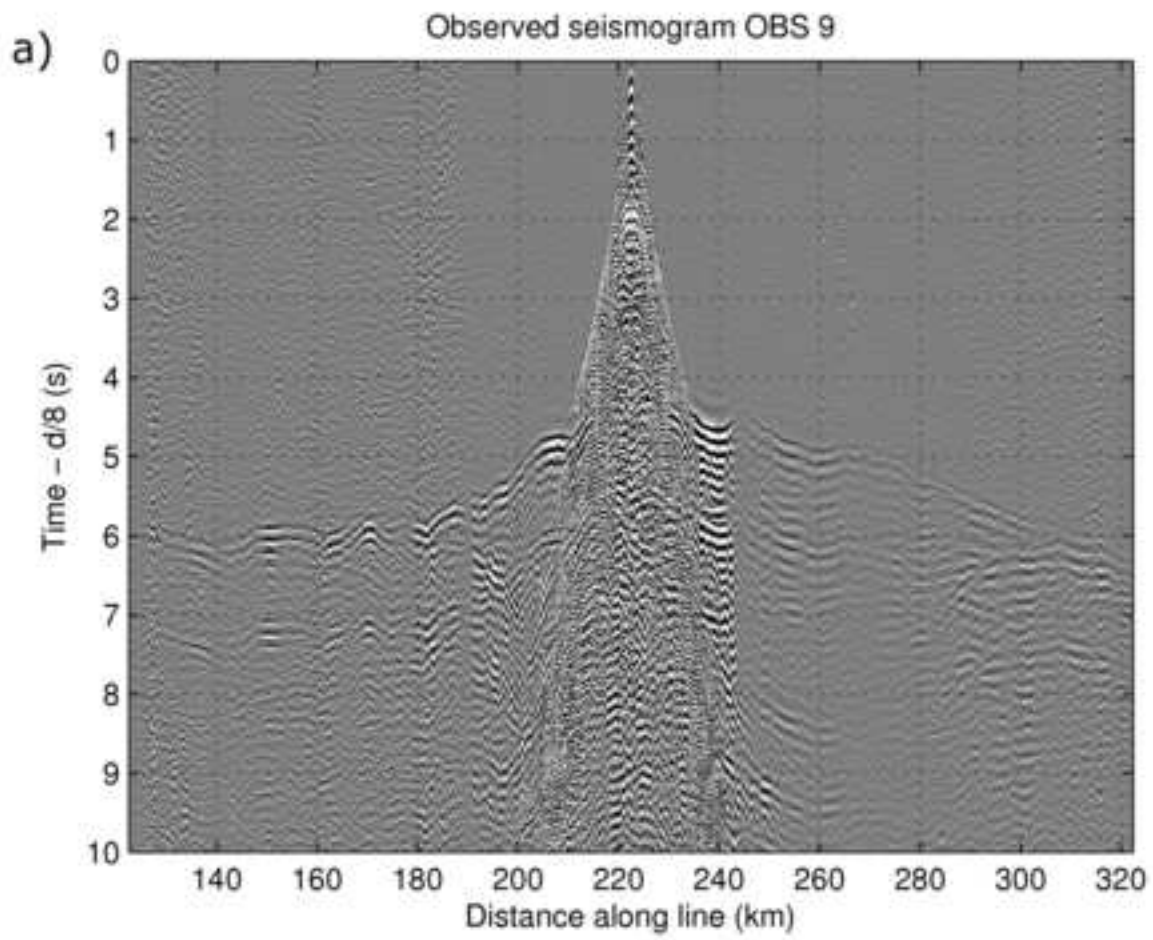


Figure 12

[Click here to download high resolution image](#)

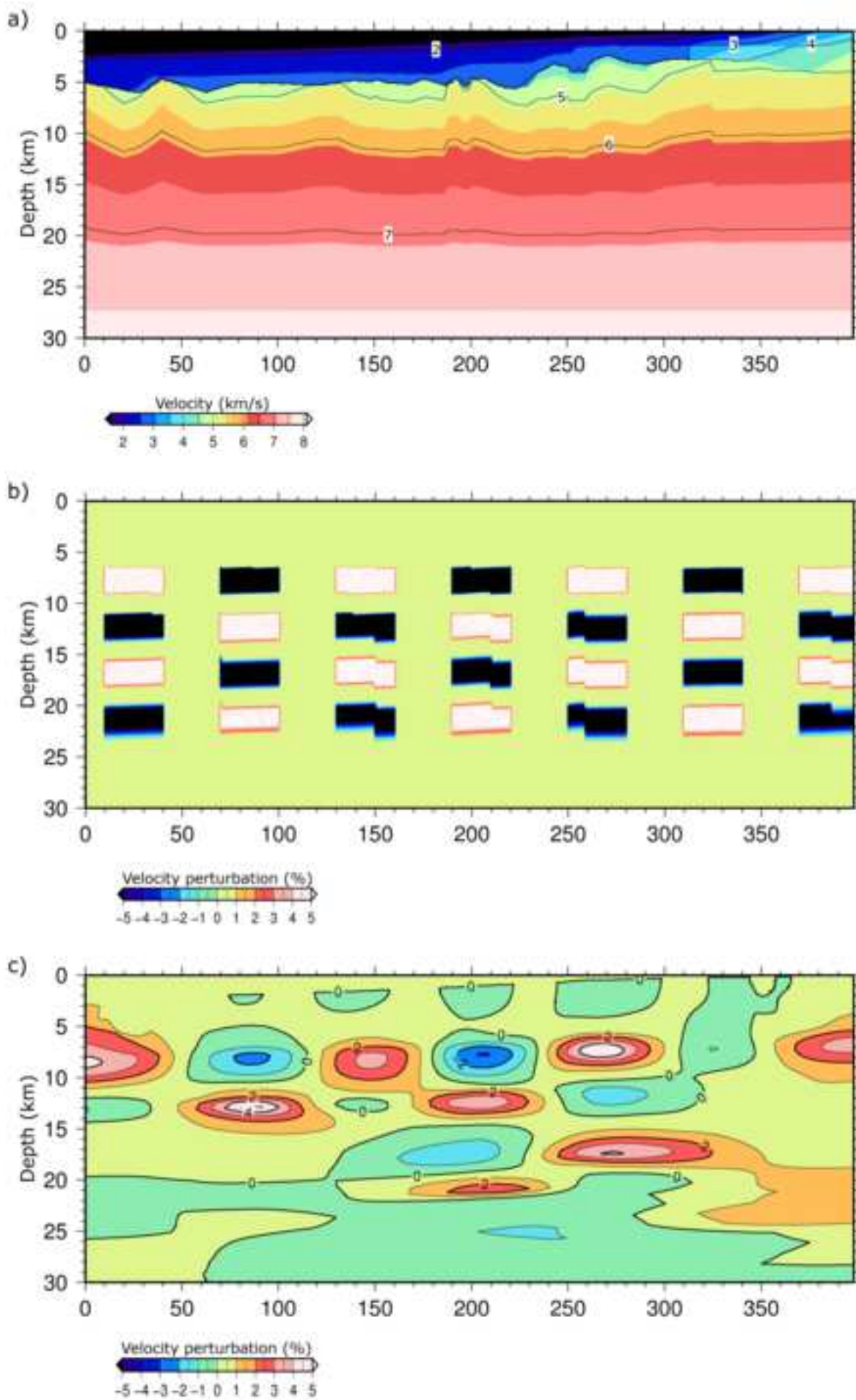


Figure 13
[Click here to download high resolution image](#)

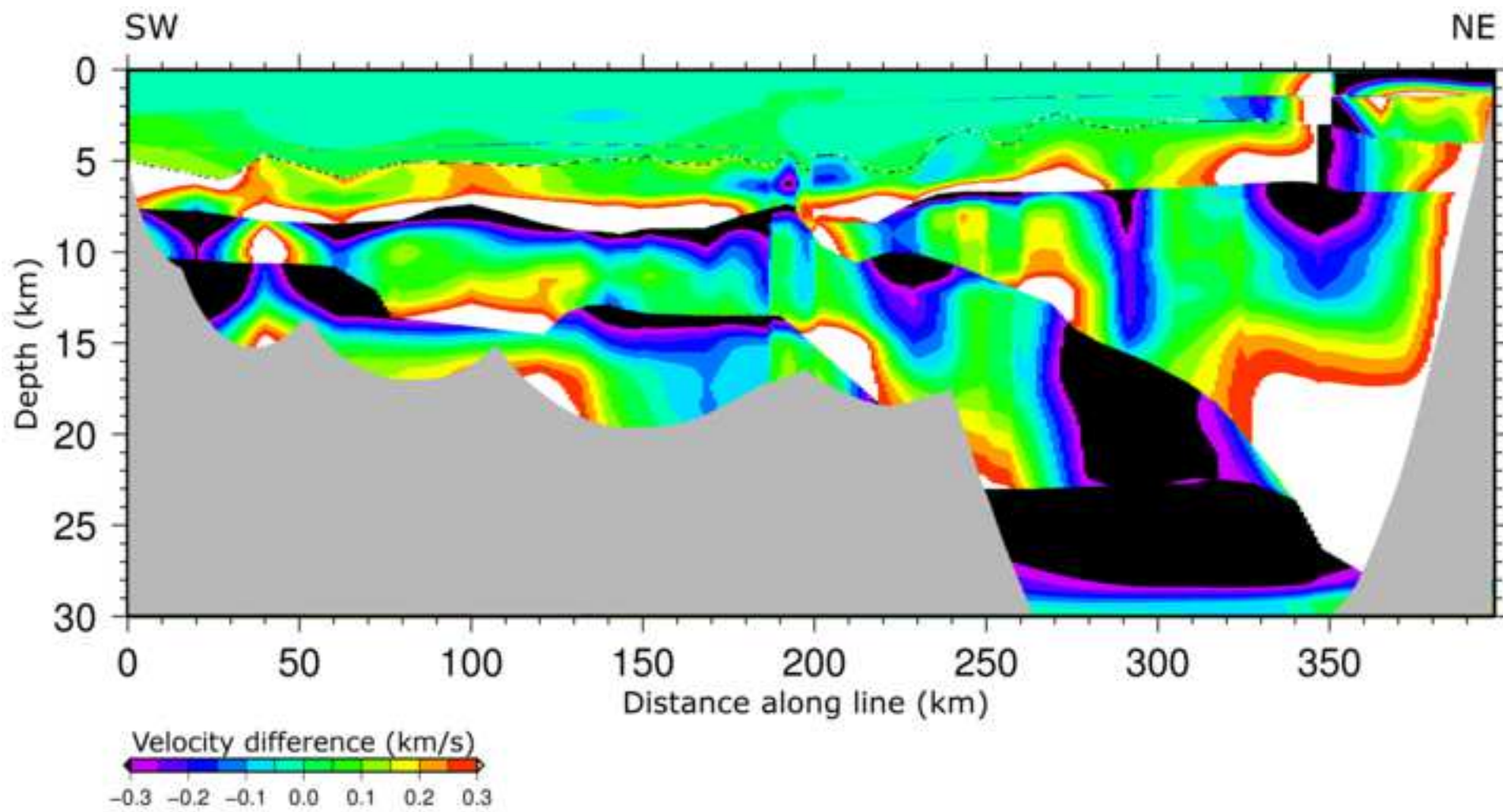


Figure 14
[Click here to download high resolution image](#)

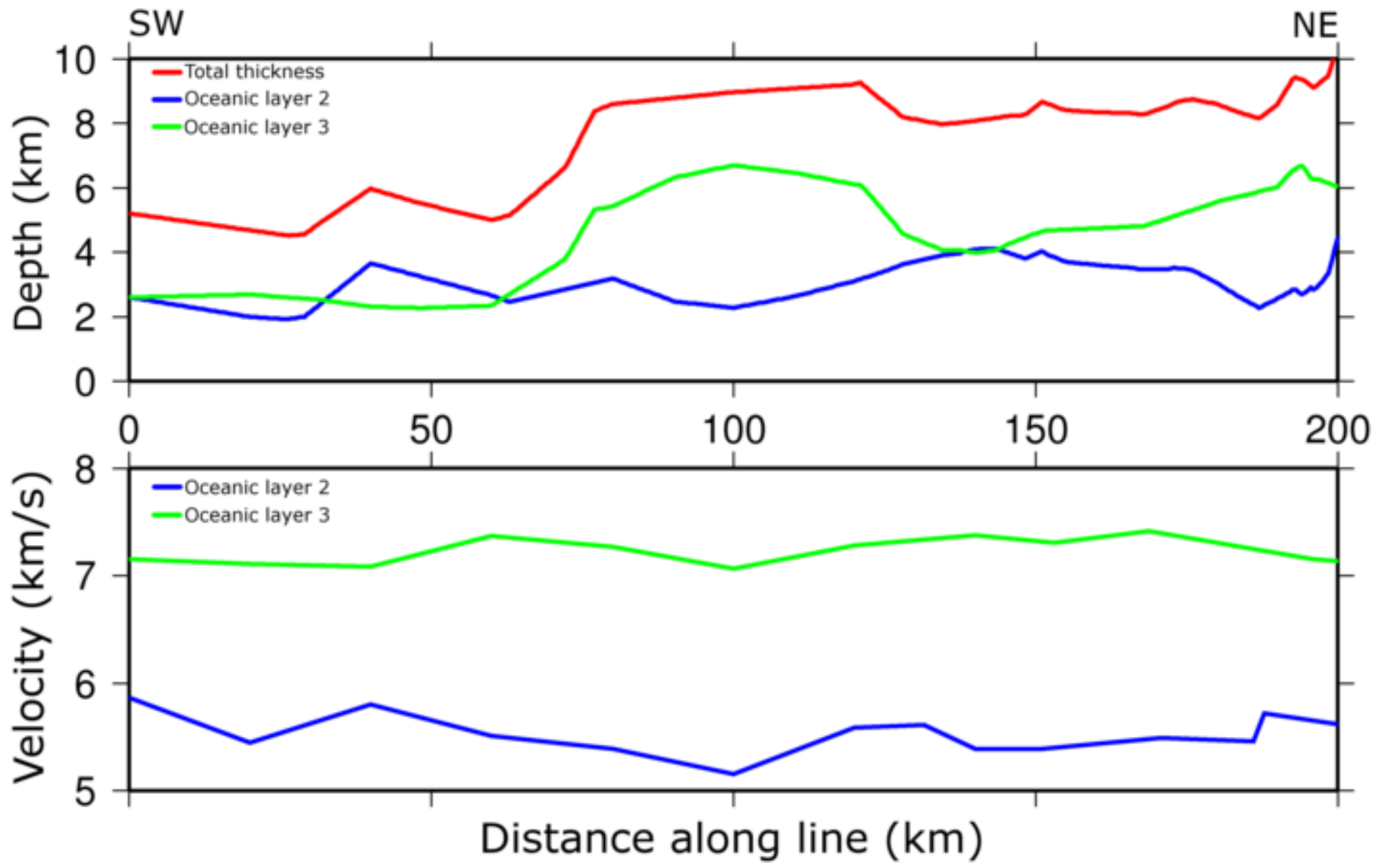


Figure 15
[Click here to download high resolution image](#)

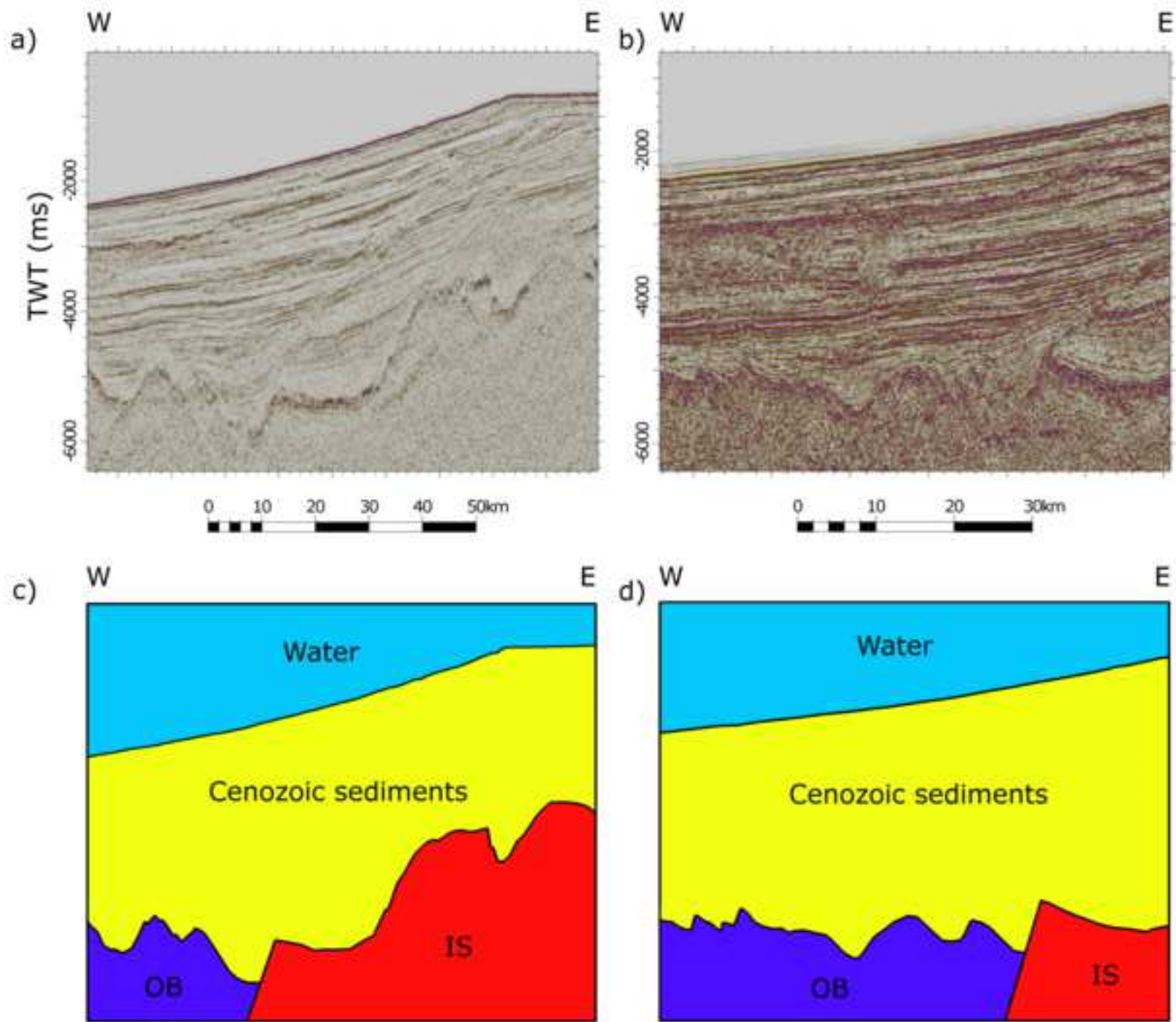
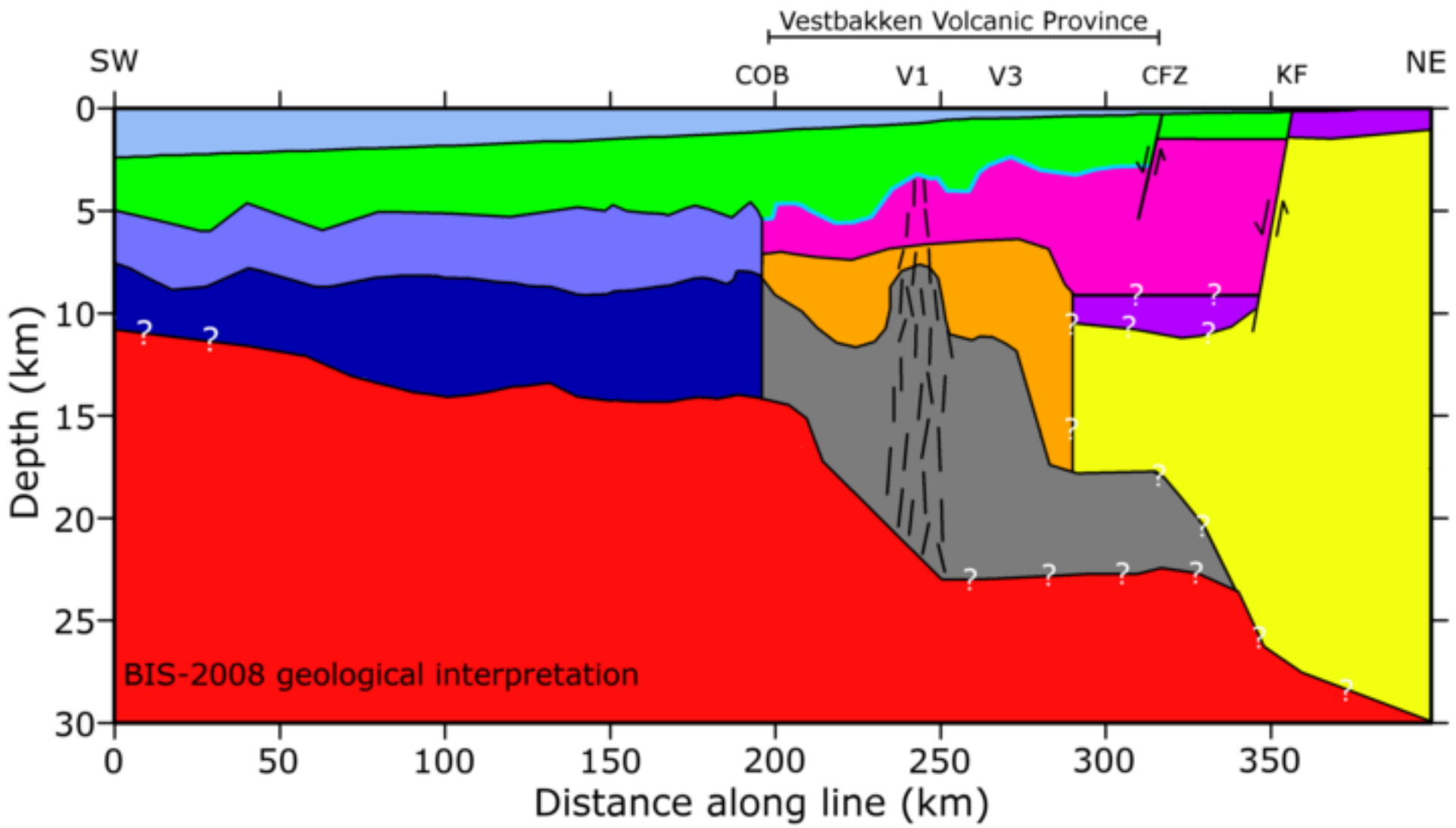


Figure 16
[Click here to download high resolution image](#)



- | | | |
|---|---|---|
|  Waterlayer |  Continental crystalline crust |  Oceanic layer 3 |
|  Cenozoic sed |  Intruded Mesozoic-Paleozoic sed and crystalline crust |  Upper mantle peridotites |
|  Mesozoic sed |  Strongly intruded lower continental crust |  Early Cenozoic mafic feeder dykes |
|  Late Paleozoic-Mesozoic sed |  Oceanic layer 2 |  Top Eocene basaltic flows or Eocene/Oligocene volcanoes |